Charles University in Prague
Faculty of Mathematics and Physics

Diploma Thesis

Miroslav Nožička

Silicon detector for detection of inelastic scattering of electrons on protons in H1 experiment

Institute of Particle and Nuclear Physics

Supervisor: Doc. Ing. Josef Žáček, DrSc.
Consultant: Dr. rer. nat. Wolfgang Lange, IfH DESY, Zeuthen

Study programme: Nuclear and Subnuclear Physics

I would like to express my gratitude to Josef Žáček, the supervisor of this diploma thesis, for his stimulating interest in the preparation of the thesis. He enabled me within the framework of the agreement between DESY–Zeuthen and the Faculty of Mathematics and Physics to participate in the upgrade of the H1 silicon trackers at DESY–Zeuthen. He helped me together with Petr Reimer, Institute of Physics, AVČR, to correct the embarrassment in the thesis text.

I am very grateful to Wolfgang Lange who supervised my thesis during my stay at Zeuthen. He explained me a lot of technical details of the hardware of the H1 silicon trackers and of the Zeuthen test facility. I thank him also for careful reading of the thesis text.

I would like to thank to Max Klein, the leader of the H1 Zeuthen group, for his steady interest in my work. He helped me to overcome various administrative problems.

I am indebted to other people of the H1 Zeuthen group who participate in the upgrade of the silicon tracker, namely Peter Kostka, Hans Henschel, Thomas Naumann, Uli Harder, Joachim Meissner and Ursula Schwind.

My gratitude belongs to Tomáš Laštovička for his friendly help especially in the first months in DESY Zeuthen and with whom I had many discussion about data analysis. I wish to thank to Ilja Tsourine who explained me a lot of details of electronics.

I greatly appreciate the financial support of the DESY–Zethen during my stay at Zeuthen. Travel and other expenses of my visits at DESY were also kindly covered by the Prague H1 group from the Charles University grant GAUK no. 173/2000.

Last but not least I would like to thank to my family and friends for steady support I had during my study at the Charles University.

Prohlašuji, že jsem svou diplomovou práci napsal samostatně a výhradně s použitím citovaných pramenů. Souhlasím se zapůjčováním práce.

V Praze, 21.8. 2000

Contents

Introduction

Lepton–hadron scattering experiments are mainly used in the high energy physics for investigation of the structure of hadrons. HERA collider at DESY, Hamburg, is the most recent facility to study the electron–proton beam collisions at high center of mass energy.

The H1 experiment was designed to provide the measurement of scattering of electrons on protons at one of the interaction zones of HERA. Since the HERA collider will be upgraded in 2001 some parts of the H1 apparatus will be modified. For instance Backward Silicon Tracker (BST) will be replaced and a new Forward Silicon Tracker (FST) will be installed in spring 2001. They will make it possible to exploit a new physics domain which will be open by the increase of the HERA luminosity.

The subject of this thesis is to present results of various tests of silicon wafers and the front end electronics which have to be performed prior to assembly of FST and BST. The thesis is organized as follows:

The first chapter gives an overview of deep inelastic scattering and methods which are most commonly employed for the determination of the momentum transfer and the inelasticity. In addition the production of heavy quarks in e–p collisions is briefly discussed.

Chapter 2 introduces HERA collider and the H1 experiment. The main components of the H1 detector and their technical aspects are explained.

The principle of microstrip detectors, the global layout of BST and FST and physics goals for which they can be used are presented in chapter 3.

The next two chapters summarize mainly the results of tests of silicon wafers and the front end electronics which have been performed during my stay at DESY–Zeuthen from September 99 to July 00. Chapter 4 gives the detailed description of silicon sensors which have three different topological patterns. Furthermore various static and dynamic checks are discussed and the quality of the fabrication of wafers is shown. The performance of the analog pipeline chips (APC128) and decoders is demonstrated in chapter 5.

The final chapter gives a summary of results.

Chapter 1

Deep Inelastic Scattering

The scattering of pointlike projectiles on atoms was first used by Ernest Rutherford who observed that the mass of atom is concentrated in a small nucleus of positive charge. Since that time scattering experiments started to evolve to nowadays form. Higher energies brought deeper view into the structure of matter and enlarged the field of physics investigations. The original Rutherford formula for a cross section was modified by taking into account other effects like projectile spins and particle structures.

In this chapter the deep inelastic scattering (DIS) is briefly outlined (for details see [2] – [8])

1.1 The DIS Kinematics

The basic Feynman diagrams for the scattering of proton on leptons are shown in Fig. 1.1. Here X denotes any hadronic final state allowed by the conservation laws and k, k' are four-momenta[1] of the corresponding particles. The special case of these processes is the *elastic scattering* where $X = proton$ and $l = l'$. An interaction where particles in the final state differ from particles in the initial state is called the *inelastic scattering*.

The inelastic scattering can proceed via two types of processes:

- **neutral current** processes (see Figure 1.1a), where the intermediate

[1]In the natural system of units, where speed of light c and the reduced Planck constant $\hbar$ are both unity, the four-momenta is defined as $p = (E, \vec{p})$. This system will be used for the rest of this thesis.

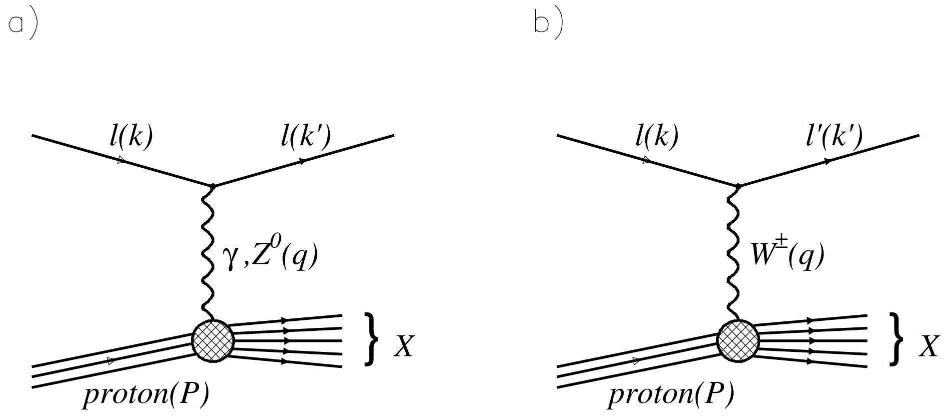

Figure 1.1: Basic Feynman diagrams for DIS a) neutral current process; b) charge current process

particle is the virtual photon γ or the virtual boson Z^0. The initial and final state leptons are the same particles.

- **charge current** processes (see Figure 1.1b), where the charges of l, l' differ by unity and the reaction is mediated by the vector boson $W^{\pm}$.

The deep inelastic scattering is commonly described by the Lorentz invariant variables

$$s \equiv (k+P)^2 \doteq 4E_e E_P \tag{1.1}$$
$$u \equiv (P-k')^2 \doteq M_P^2 - 2E_P E_e'(1+\cos\vartheta) \tag{1.2}$$
$$t \equiv -Q^2 \equiv q^2 \equiv (k-k')^2 \tag{1.3}$$
$$y \equiv \frac{q \cdot P}{k \cdot P} \tag{1.4}$$
$$x \equiv -\frac{q^2}{2q \cdot P} \tag{1.5}$$
$$W^2 \equiv (q+P)^2 \tag{1.6}$$

where E_e (E_e') means the energy of initial (final) electron, E_P is the energy of the incoming proton, M_P is the proton mass and ϑ is the angle of the scattered lepton. Variable $\sqrt{s}$ is the total energy of the colliding particles in the center of mass system (CMS), Q^2 is the negative square of the momentum transfered by the intermediate particle. The variable x denotes the fraction of energy, which carries the interacting particle inside the proton. The inelasticity y expresses the relative loss of lepton energy in the proton rest system. Variable W is the invariant mass of the hadronic system X. We talk about the "deep" inelastic scattering if the masses of the initial particles are negligible with respect to Q^2 or qP. In this case the following relation holds

$$Q^2 = s \cdot \ x \cdot y \tag{1.7}$$

The reconstruction of quantities Q^2, y, x can be done using either the measured angle and the energy of the scattered leptons only or combining them with the measurement of the hadronic system.

1.2 Reconstruction of the kinematical variables

Several methods for reconstruction of kinematical invariants Q^2, y or x has been used by DIS experiments. We will briefly outline two of them that are most commonly applied in the H1 experiment, namely the electron and the Σ method. The description of other methods as well as a comparison between them can be found in [12].

1.2.1 Electron Method

This method is based on the measurement of kinematical quantities of scattered electrons i.e. the energy E'_e and the scattering angle ϑ. It is experimentally the simplest method but can not be used in case of charge current events. The precision of the reconstruction is very good for high y region ($y > 0.2$) but rapidly degrades for lower y due to the term $1/y$ (see equation 1.12)

The kinematical variables are calculated using the relations

$$Q^2 = 4E_eE'_e \cos^2\frac{\vartheta}{2} \tag{1.8}$$

$$y = 1 - \frac{E'_e}{E_e}\sin^2\frac{\vartheta}{2} \tag{1.9}$$

The resolutions of reconstructed kinematical variables are given by following formulae.

$$\frac{\delta Q^2}{Q^2} = \frac{\delta E'_e}{E'_e} \oplus \tan\frac{\vartheta}{2} \cdot \delta\vartheta \tag{1.10}$$

$$\frac{\delta y}{y} = \frac{1-y}{y} \cdot \frac{\delta E'_e}{E'_e} \oplus \frac{\delta\vartheta}{\tan\frac{\vartheta}{2}} \tag{1.11}$$

$$\frac{\delta x}{x} = \frac{1}{y} \cdot \frac{\delta E'_e}{E'_e} \oplus (\tan\frac{\vartheta}{2} + \frac{1-y}{y} \cdot \cot\frac{\vartheta}{2}) \cdot \delta\vartheta \tag{1.12}$$

where $\oplus$ is defined via the relation $A \oplus B \equiv \sqrt{A^2 + B^2}$.

1.2.2 The Σ Method

From the measurement of the energy and momentum of the hadronic system the variable Σ defined as [12]

$$\Sigma = \sum_h (E_h - p_{z,h}) \tag{1.13}$$

can be determined. Here the index h denotes hadrons in the final state. If the measured lepton quantities and Σ are combined, the inelasticity y and Q^2 can be expressed as follows [12]

$$y_\Sigma = \frac{\Sigma}{\Sigma + E'_e(1-\cos\vartheta)} \tag{1.14}$$

$$Q^2_\Sigma = \frac{E'_e \sin^2\vartheta}{1 - y_\Sigma} \tag{1.15}$$

Using the error propagation,

$$\frac{\delta y_\Sigma}{y_\Sigma} = (1-y)\left(\frac{\delta\Sigma}{\Sigma} \oplus \frac{\delta E'_e}{E'_e} \oplus \frac{\delta\vartheta}{\tan\vartheta/2}\right) \tag{1.16}$$

we can conclude that this method gives a better precision then the electron one since there is no divergence [12] at low y.

One of the advantages of this method is that the reconstruction is independent of the initial state radiation when a photon is emitted by the initial lepton. The Σ method makes it possible to reach a good resolution in a wider kinematic region w.r.t. other methods.

1.3 DIS Cross Section and Structure Functions

The equation (1.17) represent the general formula in the first order of Feynman diagrams [6] for the spin averaged neutral current differential cross section neglecting the proton and electron masses.

$$\frac{d^2\sigma}{dxdQ^2} = \frac{2\pi\alpha}{xQ^4}\left[2xy^2F_1 + 2(1-y)F_2 + \{1-(1-y)\}^2 xF_3\right] \tag{1.17}$$

where α is the fine-structure constant.

In the naive quark model, where all quarks in the proton are massless with the spin 1/2 and don't carry any transversal momentum p_T the Callan-Gross relation holds.

$$2xF_1 = F_2 \tag{1.18}$$

In the QCD improved parton model (see [1]) this relation is violated and the F_1 can be replaced by the longitudinal structure function F_L defined as

$$F_L = F_2 - 2xF_1 \tag{1.19}$$

The differential cross section 1.17can now be modified as

$$\begin{aligned}\frac{d^2\sigma}{dxdQ^2} = \frac{2\pi\alpha}{xQ^4} \quad & [\{1+(1-y)^2\}F_2(x,Q^2) - y^2F_L(x,Q^2) + \\ & + \{1-(1-y)\}^2 xF_3(x,Q^2)]\end{aligned} \tag{1.20}$$

The form of the structure functions for higher orders of Feynman diagrams depends on the renormalization scheme. In the DIS scheme the structure functions are given by [6]

$$F_2 = \sum_{u,d,s,c,b} A_f(Q^2)\left(x\cdot q_f(x,Q^2) + \bar{q}_f(x,Q^2)\right) \tag{1.21}$$

$$F_3 = \sum_{u,d,s,c,b} B_f(Q^2)\left(x\cdot q_f(x,Q^2) - \bar{q}_f(x,Q^2)\right) \tag{1.22}$$

where q_f and $\bar{q}_f$ are the quark and antiquark distribution functions of the corresponding flavour f. Coefficients A_f and B_f include the coupling constants of the electromagnetic and weak interactions. Their dependencies on Q^2 originating from the propagator P_z of the weak interactions can be expressed by the relations:

$$A_f = e_f^2 - 2e_f c_v^e c_v^f P_Z + ({c_v^e}^2 + {c_v^f}^2)({c_a^e}^2 + {c_a^f}^2)P_Z^2 \quad (1.23)$$
$$B_f = -2e_f c_a^e c_a^f P_Z + 4c_v^e c_v^f c_a^e c_a^f P_Z^2 \quad (1.24)$$
$$P_Z = \frac{Q^2}{Q^2 + {M_Z}^2} \quad (1.25)$$
$$c_v^f = T_f - e_f \sin{\theta_W}^2 \quad (1.26)$$
$$c_a^f = T_f \quad (1.27)$$
$$\begin{aligned} T_f &= -\frac{1}{2} \qquad f = l, d, s, b \\ &= +\frac{1}{2} \qquad f = \nu, u, c, t \end{aligned} \quad (1.28)$$

where the c_v^f and c_a^f mean the electro-weak vector and axial coefficients for the fermion f, θ_W is the Weinberg mixing angle.

It is clearly visible that the structure function F_3 strongly depends on the propagator P_Z. Due to this fact F_3 contributes substantively to the cross section for Q^2 of the order of M_Z^2.

Differential cross section for neutral current interactions at $Q^2 \ll M_Z^2$ includes two structure functions F_2 and F_L. To determine them independently we have to measure the DIS cross section at different s.

1.4 Heavy flavour physics

Heavy quarks are mainly produced in photon-gluon fusion processes (see Fig. 1.2) QCD Compton scattering (see Fig. 1.2b) is negligible since the values of distribution function of heavy quark in proton are very small.

Main contribution to the production of heavy flavour quark comes from the photoproduction, i.e. when Q^2 approaches zero.

The formula for the differential cross section of the electron-proton scattering can be rewritten in terms of the scattering of the virtual photon γ^* on proton ($Q^2 \ll M_Z^2$) [1]

$$\frac{d^2\sigma}{dxdQ^2} = \frac{\alpha}{2\pi x Q^2}(1-x)\left\{\left[1 + (1-y)^2\right]\sigma_T(x, Q^2) + 2(1-y)\sigma_L(x, Q^2)\right\} \quad (1.29)$$

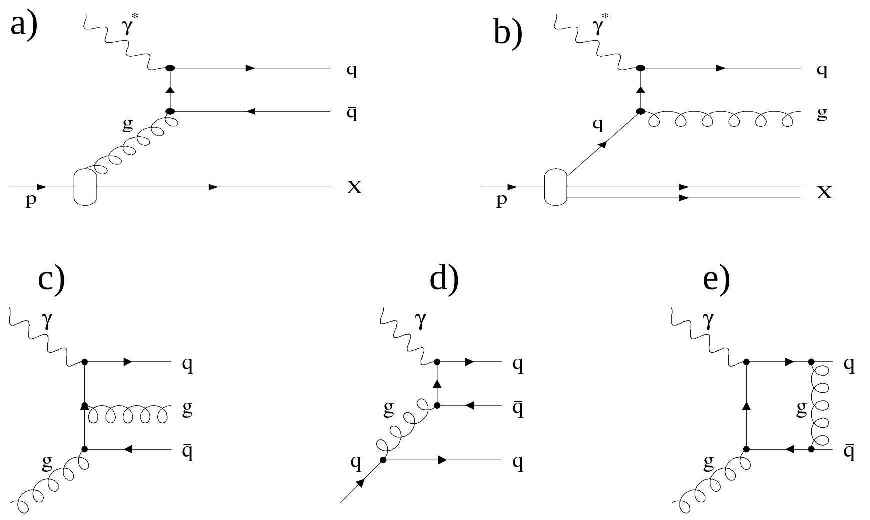

Figure 1.2: Feynman diagram of the main heavy quark production processes: a) photon–gluon fusion; b) QCD Compton process; c – e) photon gluon fusion in higher order of Feynman diagrams.

where $\sigma_T(x, Q^2)$ and $\sigma_L(x, Q^2)$ are the cross sections of the transversally resp. longitudinally polarized photon γ^*.

For a quasi real photon σ_L can be neglected. If $x \to 0$ the cross section 1.29 can be simplified

$$\frac{d^2\sigma}{dxdQ^2} = \frac{\alpha}{2\pi x Q^2}\left(1 + (1-y)^2\right)\sigma^{tot}_{\gamma^* p}(x, Q^2) \tag{1.30}$$

where $\sigma^{tot}_{\gamma^* p} = \sigma_T + \sigma_L$.

The cross section for the heavy quark production in the photon gluon fusion in the first order can be factorized into the gluon density and the photon–gluon cross section

$$\sigma^{PGF}_{\gamma p} = \int g(x_g, ...)\sigma_{\gamma g}(\hat{s}, m_q, ...)dx_g \tag{1.31}$$

The integrants depend on momentum fraction x_g carried by gluon, the mass of the produced quark and the CMS energy $\hat{s}$ of the quark pair. Measurement of this cross section provides a means to the direct determination of the gluon distribution function in proton.

Processes 1.2 c), d), e) are of higher orders. Therefore the NLO QCD calculations have to be performed to obtain their cross section. The study of the dependence of the photoproduction cross section on Q^2 allows to test QCD predictions in higher orders.

The produced heavy quarks undergo the fragmentation into hadrons. They can form the heavy quarkonia like $\mathbf{J}/\psi\,(c\bar{c})$ or $\mathbf{\Upsilon}\,(b\bar{b})$, heavy mesons, or heavy baryons. The heavy mesons decay mainly via the weak interactions. Therefore their decay lengths are rather long $D^{\pm}\,(d,c)$ $317\,\mu$m, D^0 $(\bar{u},c)$ $124\,\mu$m, $B^{\pm}\,(u,b)$ $495\,\mu$m and $B^0\,(d,\bar{b})$ $468\,\mu$m [16].

The decay widths are proportional to the elements of the Cabbibo–Kobayashi–Maskawa matrix (CKM) that are fundamental parameters within the Standard model. The dominant decays of the heavy quarks are then:

$$b \to c\,W^- \qquad\qquad c \to s\,W^+ \tag{1.32}$$

The virtual W mesons decay either into lepton–neutrino pair or hadronically into a quark–antiquark pair.

A precise spectroscopy of the heavy flavour quarks provides the access to a number of interesting physics issues:

- study of the mixing of neutral D and B mesons. The mixing rate is small in the charm sector compared to the K^0 or B^0 mesons and the process $D^0 \to \bar{D}^0 \to K^+\pi^-$ has the same final state as the doubly Cabibbo suppressed D^0 decay. The processes can be distinguished by measuring the secondary vertices distributions. Therefore the vertex resolution $\approx 50\,\mu$m ($\approx 0.5 \cdot \tau_{D_0}$) is needed.

- the extraction of the gluon density [17].

- the determination of the b–quark production cross section [18].

Chapter 2

H1 Detector

In this chapter the HERA accelerator and the H1 detector is briefly described. A complete overview of the detector as well as a description of magnets, luminosity system, triggers, data acquisition, off–line data handling and simulation can be found in [9, 10].

2.1 HERA accelerator

The H1 detector is installed at HERA collider in DESY–Hamburg, which is a hadron–electron ring accelerator facility of the length of 6336 m with four interaction zones. They house two colliding experiments (H1, ZEUS) and two fixed target experiments (Hermes, HERA–B).

The energies of lepton (e^+ or e^-) and proton beams reach values of 27.55 and 920 GeV respectively. The beam injection into HERA is done in steps involving several preaccelerators (see Fig. 2.1). The transversal dimensions of the lepton and proton beams in the vertical direction are $50\,\mu$m and in the horizontal direction about $270\,\mu$m. The lepton and proton bunch lengths are 0.83 cm and 8.5 cm.

2.2 H1 Detector

H1 detector was build in the north hall of the HERA collider in 1992. Since the energy of electrons is lower than the energy of protons most of secondary particles move in the proton direction. Therefore the H1 apparatus is asymmetric in the longitudinal direction (r–z plane) (see Fig. 2.2).

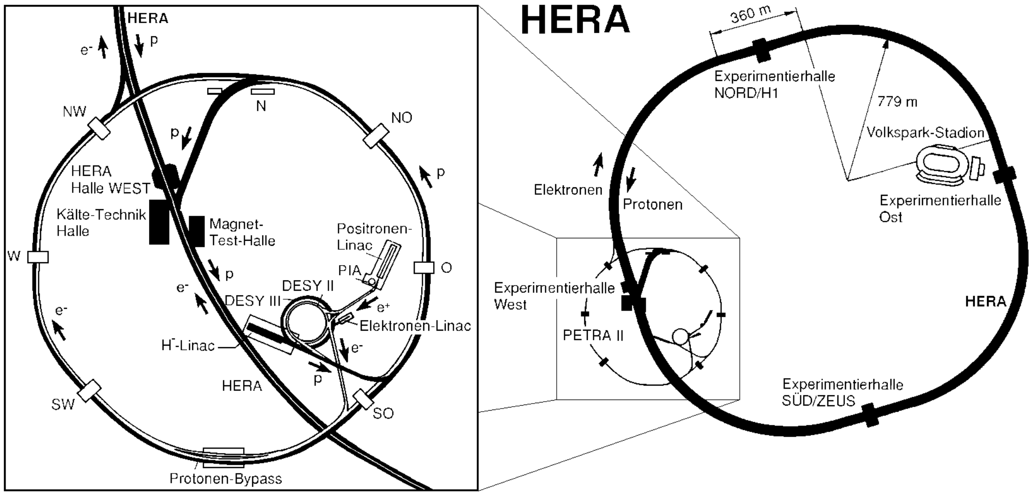

Figure 2.1: The HERA accelerator with the system of preaccelerators and placement of interaction zones.

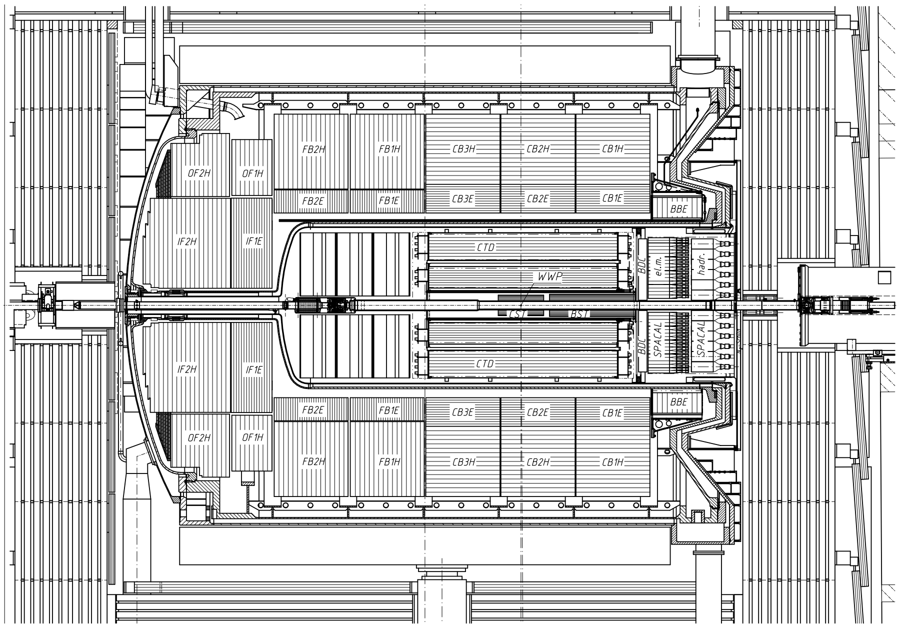

Figure 2.2: Schematic layout of the H1 detector

The center of reference system is situated in the nominal interaction vertex with the positive z-axis in the direction of the proton beam. The H1 detector has three main parts: Central region, which is centered around the Central Silicon tracker, Backward region in the $-z$ direction and Forward region in the $+z$ direction. It has a number of subdetectors which ensure the tracking, particle identification, energy measurement and the detection of muons. The main detectors are complemented with a luminosity system which serves mainly for online and absolute luminosity measurement. Every event is validated by a system of triggers.

All detectors except the muon system are surrounded by the superconducting coil producing magnetic field parallel with the collider tube of 1.15 T in average.

2.2.1 Tracking system

The H1 tracking system provides the track reconstruction and particle identification of each triggered event. Track detectors measure the transversal momentum with precision of $\sigma_p/p_T^2 \approx 3\times10^{-3}GeV^{-1}$. They are also included in many H1 triggers [10]. The whole tracking system covers the angular region $8° < \theta < 173°$. Resolution of the angle reconstruction is dependent on individual subdetectors and is $\sigma_\theta \approx 1$ mrad on average.

Tracking system has three main parts: central and forward tracker and the backward drift chamber.

- **The central tracker** includes the central jet chambers (CJC1, CJC2) central z–chambers (CIZ, COZ), central proportional chambers (CIP, COP) and central silicon tracker (CST).

  Central jet chambers CJC1 and CJC2 which are gas like drift chambers consisting of 30 respectively 60 cells are inclined by about 30° to the radial direction. Anode sense wires are strung parallel to the beam pipe along the whole length of the chambers. In the longitudinal plane (r–z) the active length of the cells is 2.2 m. The spatial resolution is 170 μm and 2.2 cm in the transversal and z–direction. These chambers provide also the particle identification based on the energy ionization losses with a precision $\sigma_{dE/dx} = 10\%$.

  Central z–chambers complement charged particle track and momentum measurements. The inner chamber (CIZ) has 15 rings and 16 cells per ring and measures the z–position with precision of 0.26 mm. The outer chamber (COZ) consists from 25 cells per ring and has 24 rings that give together length of 2.16 m and provide measurement with an accuracy of 0.2 mm. The chambers cover the polar angular region $16^\circ < \theta < 169^\circ$ and $25^\circ < \theta < 156^\circ$ respectively.

Central proportional chambers are used for the triggering since their time resolution is better than 96 ns, which is the time interval between bunch crossings at HERA. The central inner proportional chamber (CIP) is placed closer to the beam pipe than CIZ and cover the angular region of $9^\circ < \theta < 171^\circ$ whereas the central outer proportional chamber (COP), which is placed above COZ, has an angular acceptance of $25^\circ < \theta < 155^\circ$. The CIP (COP) chamber has 8 (16) sectors in the transversal plane and 60 (18) in the z–direction.

Central Silicon Tracker is designed to measure precisely the interaction vertex position. It is placed very close to the beam pipe. It consists of two concentric layers formed from 12 and 20 silicon ladders (see Fig. 2.3) at radii 5.75 cm and 9.75 cm respectively. The active length of one ladder is 35.6 cm and the total length of the CST is 44.2 cm. One ladder consists of six silicon sensors and hybrids with the same readout elements as those which are used for the backward and forward silicon trackers (BST/FST) hybrids (see chapter 5). The ladders are tangentially shifted to ensure an overlap in $r\phi$ of adjacent active areas. Resolution of this detector varies from $12\,\mu$m to $23\,\mu$m. The angular acceptance is about $18^\circ < \theta < 162^\circ$[1]

- **Forward tracker**(FTD) is designed to provide an accurate measurement of charged particle tracks and transversal momenta with the precision of $\sigma_{\theta,\phi} < 1\,\mathrm{mrad}$ and $\sigma_{p_T}/p^2 < 0.003\,\mathrm{GeV}^{-1}$, and to give a fast triggering in the forward part of H1 detector. It consists of three types of chambers: planar drift chambers, forward proportional chambers (FWPC) and radial chambers. A transition radiator is placed between the FWPC and the radial chamber. These parts together compose one supermodule of z–width of 422 mm. The whole forward tracker is

[1] Requiring the particle to pass both layers the angular coverage is lower $29^\circ < \theta < 151^\circ$

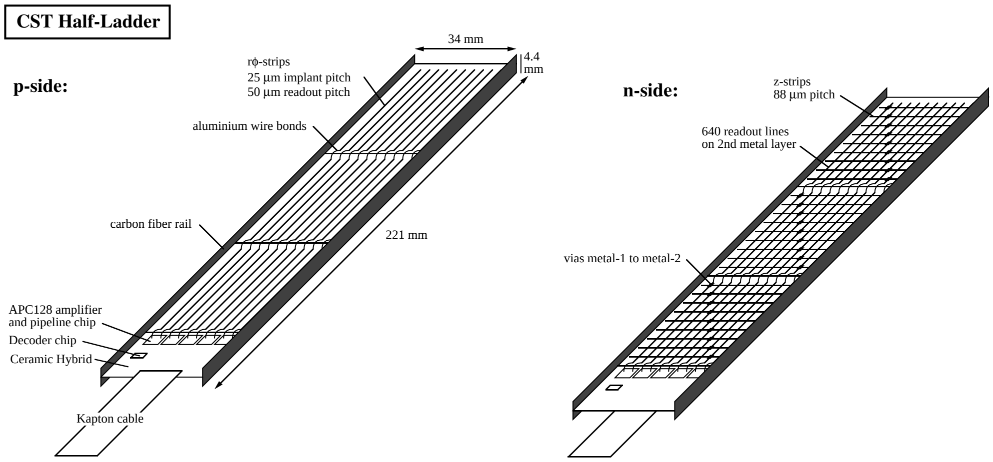

Figure 2.3: Drawing of the CST silicon ladders.

constructed of three such supermodules. The angular coverage of the forward tracker is $7° < \theta < 25°$.

- **Backward drift chamber**(BDC) is mainly used for electron identification in the backward calorimeter. It consists of four double–layer wheels divided into octants. The sense wires are strung perpendicular to the beam pipe, their distances and lengths increase with the distance from the beam pipe. This chamber complements the reconstruction of angle θ of energy clusters deposited in the backward calorimeter.

The remaining tracking detectors BST and FST will be described in detail in the next chapters.

2.2.2 Calorimeter Detectors

The H1 experiment has two main calorimeters. **Liquid Argon Calorimeter**, which is designed to measure energies of particles moving into the forward and central direction and the **Spaghetti calorimeter (SPACAL)** placed in the backward region. Both calorimeters have the electromagnetic part closer to the vertex followed by the hadronic part. There are also other calorimeters i.e. plug calorimeter, tail catcher, VLQ and FNC.

Liquid Argon Calorimeter

This calorimeter is built from eight individual wheels which are divided into eight parts. The cells filled with the liquid argon are separated with the lead or iron absorbers. The resolution of the energy reconstruction is about: $11\,\%/\sqrt{E_e} \oplus 1\,\%$, and $50\,\%/\sqrt{E_e} \oplus 2\,\%$ for electromagnetic and hadronic section respectively. For other details see [9].

Spacal

Spaghetti calorimeter [11] is placed in the backward region of the H1 detector. It makes possible to determine the $e^{\pm}$ energies with an accuracy of $7\%/\sqrt{E}$. The electromagnetic part consists of 1192 cells which have polystyrene-based scintillating fibers parallel to the beam pipe which are fixed in lead sheets. The lead to fiber ratio is 2.3:1. Each cell is 25 cm long with the square base of $40.5 \times 40.5\,\mathrm{mm}^2$ except inner cells surrounding the beam pipe. The fibers from each cell are bounded together into a cone and blue light from fibers is transmitted through a light mixer to a photomultiplier.

The hadronic part has 136 cells of the same length like the electromagnetic cells with the rectangular intersection $119.3 \times 119.0\,\mathrm{mm}^2$. The ratio between lead and fiber volume is higher (3.4:1).

2.2.3 H1 trigger system

The task of the trigger system is to select the events originating from e–p interactions out of the flow of signals registered in detectors and to reject the background signals e.g. cosmic muons, beam gas interactions and synchrotron radiation. The triggers are based on the event topology, energy depositions, interaction vertex position and particle arrival times.

The H1 trigger system consists of three levels L1, L2 and L4. The first level trigger (L1) is a dead-time free system based on up to 128 subtriggers. Since its decision comes after $2.5\,\mu$s the complete subdetector informations are stored in pipelines. The second level trigger (L2) validates the L1 decision within $20\,\mu$s using more complicated algorithms (neural network and topological trigger). Upon the positive L2 trigger decision the complete readout is started. The fourth level trigger (L4) acts asynchronously on the full data to reduce the data volume. An additional background suppression is performed here and the events are written on "raw" tapes. At the level five

(L5) the full physical event reconstruction is performed and the events are classified in analysis dependent way and are written to Data Summary Tapes (DST).

2.3 Upgrade of HERA and the H1 detector

The HERA collider will be upgraded in the second half of year 2000 and at the beginning of 2001. The main goal of the upgrade is to increase the luminosity [14]).

Luminosity upgrade

The HERA luminosity will increase approximately to value of at least $7.6 \cdot 10^{31}\, cm^{-2}s^{-1}$. This value will be reached by means of focusing super–conducting magnets which will be placed near the nominal vertex point inside the H1 detector. The transversal diameter of both beams are designed to be $118\,\mu$m horizontal one and $32\,\mu$m vertical at the beam currents 58 mA for electrons and 140 mA for protons.

The accelerator changes has an impact on the upgrade of the H1 detector.

Upgrade of the H1 detector

Two of focusing magnets of the lengths 1.75 m and 1.45 m. will be installed in the backward region. The third longest magnet will be placed in the forward part of H1 detector. Therefore an rearrangement of the inner part of SPACAL and the forward tracker is necessary. The beam pipe will be of elliptical shape in the intersection. Therefore the CST and also the BST has been redesigned (see chapter 3). A new forward silicon tracker (FST) will be installed (Detail description can be found in the next chapter). Several triggers have to be adapted due to higher HERA luminosity and a BST trigger will be included in the H1 trigger system.

Chapter 3

Backward and Forward Silicon Trackers at H1

3.1 Short Introduction to Silicon detectors

The operating principle of silicon detectors is based on ionization effects when charged particles pass through semiconductor material. The basics of semiconductor properties and some principles for using semiconductors in the detection of charged particles will be shortly outlined in this section. There is a variety of types of semiconductor detectors which are used in high energy physics. This section is mainly focused on silicon tracking detectors. A detailed overview of principles and basics of other types of semiconductor detectors can be found in [15].

3.1.1 Semiconductors and their properties

All semiconductors are crystalline materials with four valence electrons in the atomic shell. A pure semiconductor at a temperature of 0 K is an insulator with an energy gap between conduction and valence bands of about 1 eV . The conductivity increases with temperature due to the thermal break of bindings when free electrons and holes are generated in pairs. An increase of conductivity is also caused by distortions and impurities in the crystalline lattice. To obtain conductive semiconductor material either pentavalent elements (donors) or trivalent elements (acceptors) are implanted into the crystalline lattice.

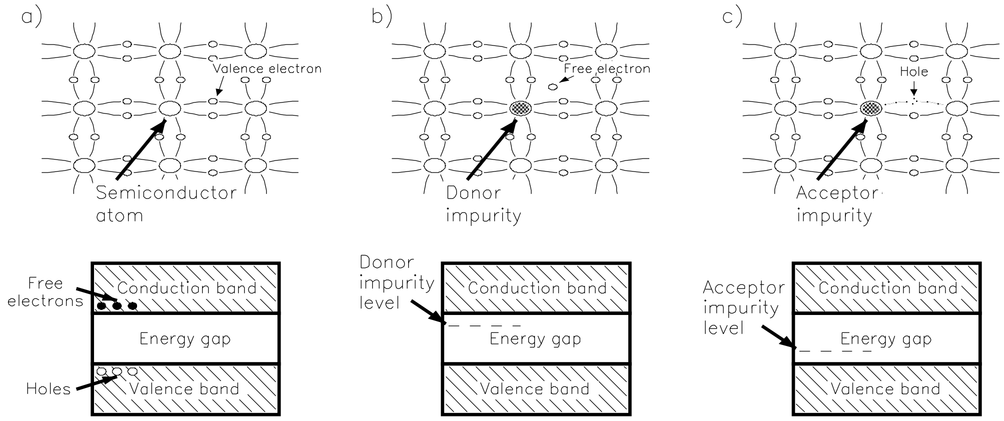

Figure 3.1: Structure of the semiconductor crystalline lattice and the energy bands: a) pure semiconductor, b) semiconductor with donor c) semiconductor with acceptor

In case of the addition of donors one electron is left over. This electron resides in a discrete energy level created in the energy gap by the presence of the impurity atom. The created level is extremely close to the conduction band (about 0.05 eV for silicon) which leads to conductivity at normal temperatures. The electron can be easily excited to the conduction band with creation of a hole. Such holes are called minority carriers. A semiconductor with electron conductivity is called *n-type* semiconductor.

If the impurity is trivalent there is an excess of holes in the crystal causing a perturbation of band structure by creating an additional state in the energy gap, which is closer to the valence band as shown in Fig. 3.1. Such a semiconductor with hole conductivity is called *p–type* semiconductor.

3.1.2 Semiconductor detectors

The functionality of all semiconductor detectors is based on the formation of *pn* junction known as semiconductor diode. Without an external potential there is an excess of free electrons in the n–type semiconductor and an excess of positive holes in the p–type. The electrons drift into the p–type silicon

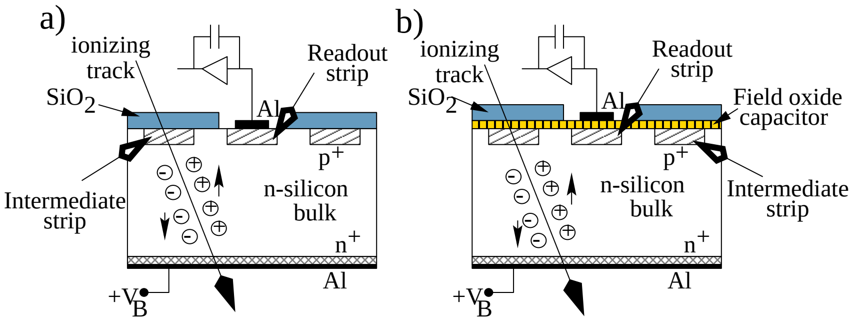

Figure 3.2: Schematic view of the passage of a particle through a semiconductor detector with readout elements a) DC coupled readout b) AC coupled readout.

to recombine there with holes and vice versa. This process forms a depleted volume at the interface between these layers causing an electric field which creates a potential difference across the junction known as contact potential.

The width of the depleted volume d is dependent on the densities of dopants N_A acceptors and N_D donors via the relation:

$$d = \sqrt{\frac{2\varepsilon V_0}{e}\frac{N_A + N_D}{N_A N_D}} \tag{3.1}$$

where ε is the dielectric constant of the material, e is the elementary charge and V_0 is the contact potential.

Without external potential the depth of the depletion zone is very small. It may be expanded with a bias voltage with its negative pole connected to the p–type and its positive pole connected to the n–type semiconductor. Since the voltage V_B is usually much higher than the contact potential V_0 the depleted layer is deeper and it can be used for detection of charged particles.

Semiconductor with enrichment of dopants are used for contacts because the direct contact with metal creates a metal–semiconductor junction (so called Schottky contact).

Particles penetrating the semiconductor generate electron–hole pairs in the semiconductor. The electrons start to drift to the n^+ layer whereas holes drift to the p^+ electrode as shown in Fig. 3.2. Such a semiconductor diode connected in reverse direction builds up a capacitor. The drifting of the electrons and holes will induce a charge on the capacitor electrodes, which may be registered and amplified with a charge-sensitive preamplifier (see Fig. 3.2) placed as close as possible to the detector to avoid parasitic capacitances. Assuming two parallel electrodes, independence of the charge carrier mobilities from the electric field and $N_D \ll N_A$, then the time dependence of charge induction from the drift of one electron–hole pair is given by the following formula:

$$Q(t) = Q_e(t) + Q_h(t) = \frac{e}{d} x_0 \left(\exp \frac{\sigma}{\varepsilon} t - \exp \frac{\mu_e}{\mu_h} t \right) \tag{3.2}$$

where μ_e,μ_h are the mobilities of electrons and holes, σ is the material conductivity, x_0 denotes the point where the electron-hole pair was created (the scale begins on cathode), e is the elementary charge and $Q_e(t)$, $Q_h(t)$ are the charges induced separately from electrons and holes.

Microstrip detectors composed of separate strips are usually made of high resistivity n–type silicon on which p^+ doped strips are implanted. An n^+ layer is implanted on the opposite side. The electrical connection is provided by aluminium strips. Typically only every third or second strip is read out, which is AC or DC coupled to the readout electronics (see Fig. 3.2). The thickness of such detectors is about 300 μm which corresponds to 25000 of electron–hole pairs created by a minimum ionizing particle passing the detector perpendicularly. The average energy needed to create an electron–hole pair at room temperature is 3.62 eV[1]. The time of charge collection is less than 10 ns.

If a particle passes the strip detector perpendicularly the charge is collected in one or two strips only. Due to the channel cross talk caused by the capacitances between neighbouring strips a small signal is visible on strips surrounding the hit strip too.

The implicit resolution dx of a general strip detector is given by the equation

$$dx = \frac{l}{\sqrt{12}} \tag{3.3}$$

where l is the distance between the strips. By means of charge division a resolution of 5 μm can be achieved with a readout strip distance of $l = 60\,\mu$m. The actual resolution depends moreover on the signal to noise ratio.

[1]Since the energy gap is of the order 1 eV two thirds of the deposited radiation energy are spent on exciting lattice vibrations.

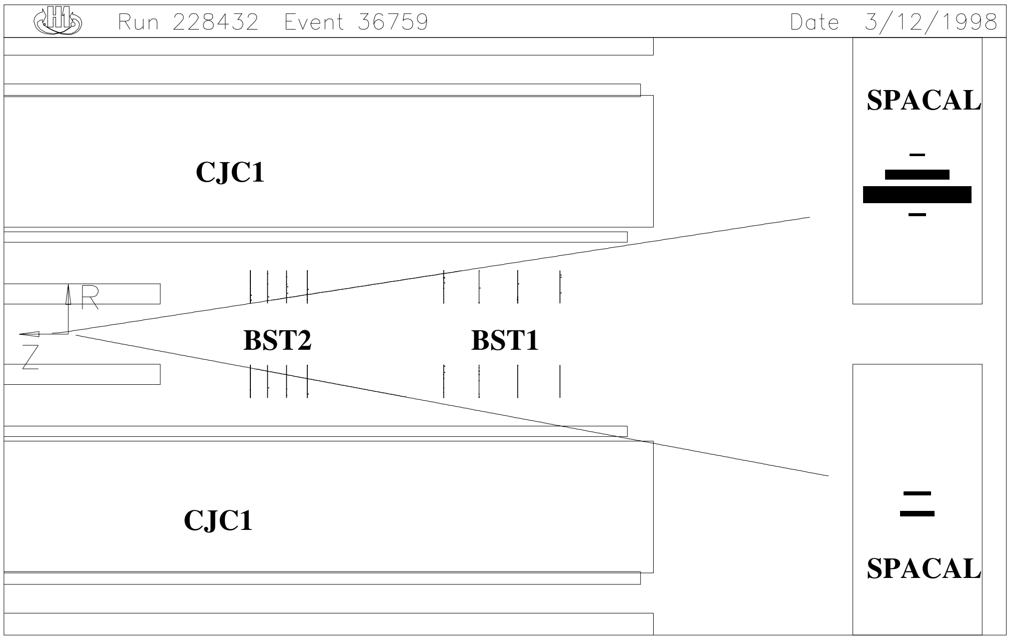

Figure 3.3: Side view of an event triggered by the SPACAL energy cluster, which is linked to the track of about 300 MeV transverse momentum (reconstructed using the BST1 and BST2).

3.2 The Backward Silicon Tracker (BST)

The Backward Silicon Tracker is designed to measure both coordinates (radius r and azimuth ϕ) of the tracks of scattered particles, in order to perform a precise measurement of the deep inelastic cross section up to large y and to extend the analysis of beauty and charm particle production towards low x.

The first part of the Backward silicon tracker, BST1, has been installed in 1995. It consists of four wheels with r–strip detector modules (16 on each wheel). In 1997 additional four wheels with r–detectors, BST2, were mounted to the BST1 closer to the interaction vertex. In 1998 eight ϕ–strip modules -one per wheel- were added. The BST1 and BST2 enlarge the acceptance of the charged particle track reconstruction since they are placed in the region where there are no other trackers. An example of the event taken during the running period in 1998 is displayed in Fig. 3.3. Without BST this type of events could not be used in the data analysis. Due to the upgrade of

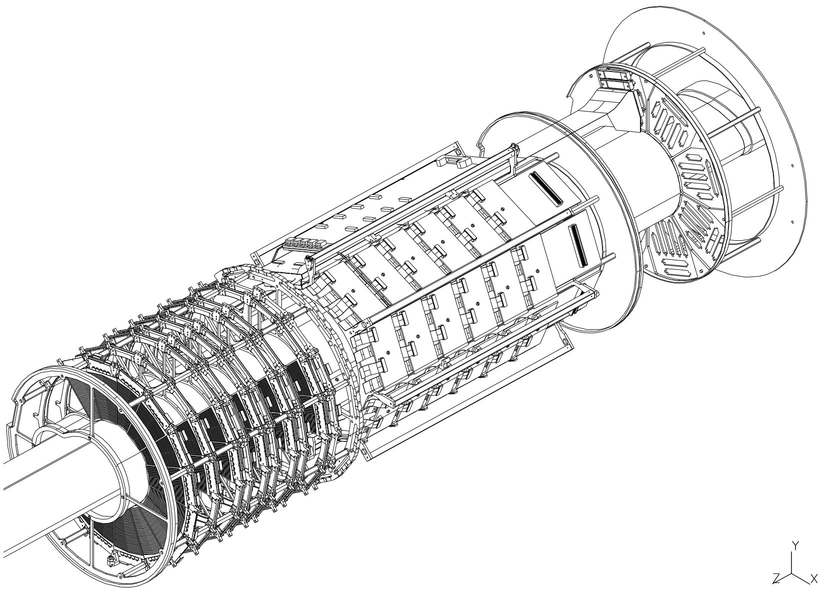

Figure 3.4: Backward silicon tracker global view.

HERA collider the BST1 and BST2 will have to be replaced. The redesigned detector BST3 is described in detail in this section.

3.2.1 Detector Layout

The BST3 will consist of 6 planes equipped with detector modules. Each module consists of a sensor containing the silicon structure and a hybrid with readout electronics. The sensors are of three types, two of them have strip pattern with arc shaped strips (r strips) and vertical strips (ϕ strips). The reamining type has a pad structure. r and ϕ–strip modules are mounted back to back. The detector part closer to the SPACAL will not be covered by the CIP trigger. Therefore the BST will also carry four wheels with pad detectors for triggering on particle tracks pointing to the vertex and for rejection of proton induced background. The positions of the wheels are given in table 3.1.

Each BST3 wheel has 8 sectors. Two sectors are left empty to adapt to the elliptical beam pipe. This gap will be used for cooling cables and radiation sensors. All other sectors will be equipped with detector modules (two in each sector on each side of the wheel) which overlap to avoid “cracks”

z – position mm	**Detector type**
384.2	$r,\ \phi$
421.2	$r,\ \phi$
461.2	$r,\ \phi$
477.2	pad
504.2	$r,\ \phi$
520.2	pad
551.2	$r,\ \phi$
568.2	pad
604.2	$r,\ \phi$
620.2	pad

Table 3.1: Distance of BST wheels from vertex.

caused by a non sensitive volume at the module borders.

The r–detectors will face the vertex; ϕ and pad detectors will be oriented to the opposite side. A detailed description of the sensors can be found in chapter 4. Looking from the vertex the readout elements consisting of six repeater motherboards will be placed behind the active detectors modules. They are connected to the contact ring which interfaces all external cables. The overall length of this detector is around 103 cm. The "active volume" occupies only 27 cm. The remainder is used by the frame and by the readout elements. The inner and outer active radii are determined by the active areas of the detector sensors ($5.9\,\mathrm{cm} \leq \mathrm{r} \leq 12.0\,\mathrm{cm}$). The maximal θ angular coverage for is between 163° and 174°.

The readout units placed on the hybrid (see 5) need to be cooled. The cooling will be built into the wheels. The coupling between the cooling system and the hybrids will be improved by an aluminium surface.

3.2.2 Resolution of the BST

The calculated resolutions from equation 3.3 are $27.7\,\mu$m for r and $21.7\,\mu$m for ϕ coordinate.

The measured resolution of BST2 has been found to be better (see Fig. 3.6). The result was obtained with the following method: The differences between measured r_m and fitted r_f values were plotted in histograms weighted

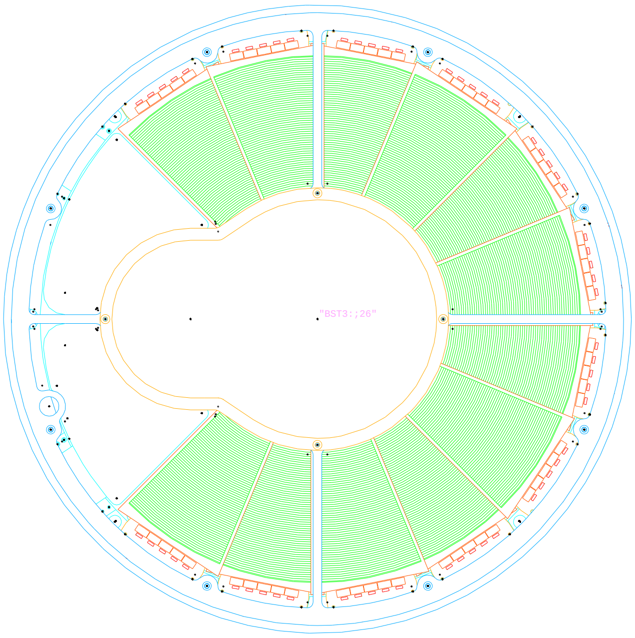

Figure 3.5: View onto one BST3 wheel equipped with detectors

accordingly to the z positions of the corresponding wheels. The geometrical weights g_j are given by the formula [19]

$$g_j = N \left\{ \sum_{k=1}^{n} \left[\langle z^2 \rangle - \langle z \rangle (z_k + z_j) + n z_k z_j - \delta_{jk} N \right]^2 \right\}^{-1/2} \tag{3.4}$$

where

$$\begin{aligned} \langle z \rangle &= \sum_{i=1}^{n} z_i \\ \langle z^2 \rangle &= \sum_{i=1}^{n} z_i^2 \\ N &= \langle z^2 \rangle - \langle z \rangle^2 \end{aligned} \tag{3.5}$$

where n is the number of hits used in the linear fit, z_j denotes the z–position of the corresponding residual for which the weight is calculated and z_k are the z–positions of the other hits in the track. The histograms were than fitted with a Gaussian curve. The standard deviation of the Gaussian distribution corresponds to the resolution of the detectors.

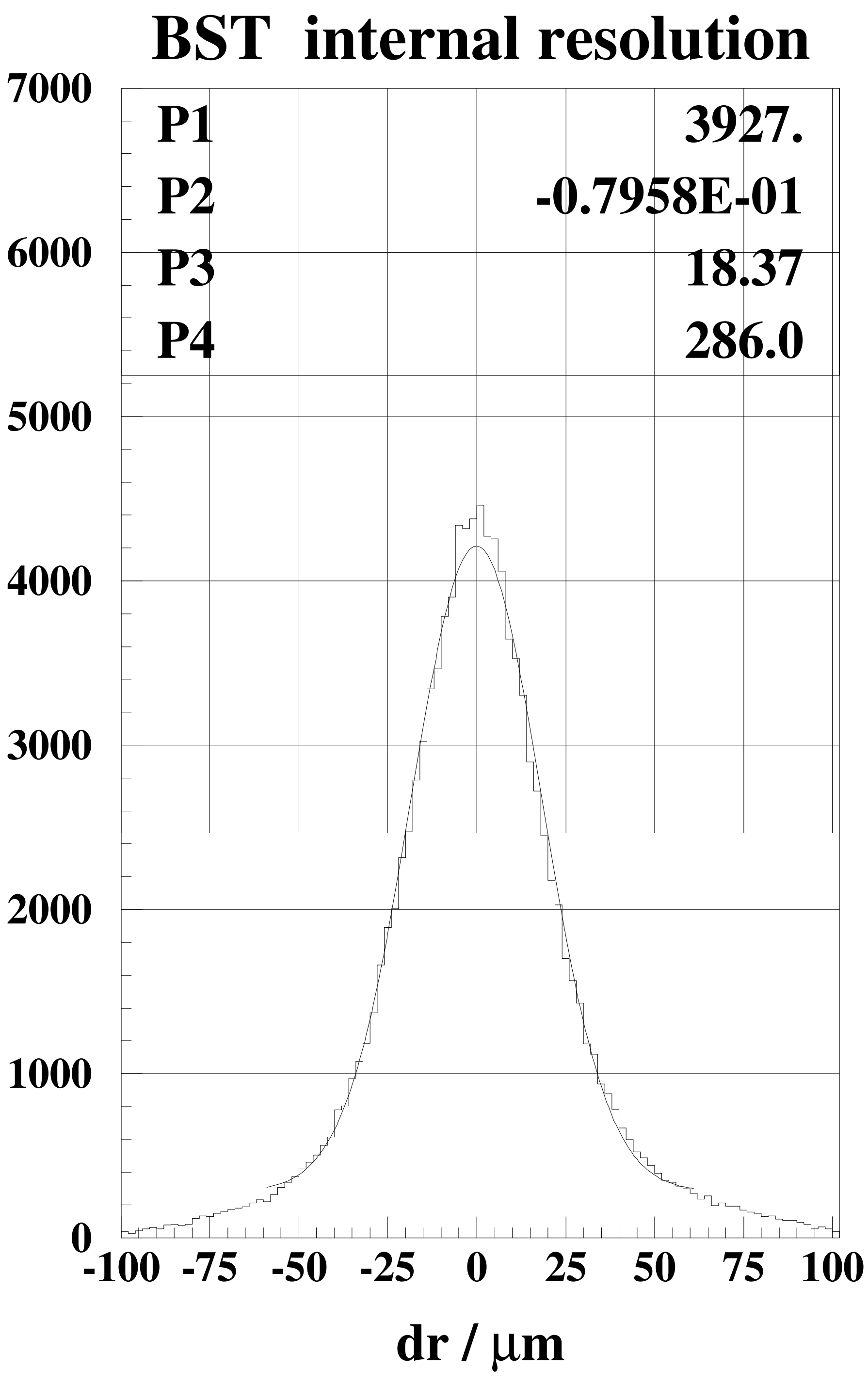

Figure 3.6: Internal resolution of r detector modules. The histogram was fitted to the formula $c = \mathbf{P}_4 + \mathbf{P}_1 \exp -\frac{(r-\mathbf{P}_2)^2}{2\mathbf{P}_3{}^2}$. The parameter $\mathbf{P}_3$ denotes the internal resolution of the r detector modules

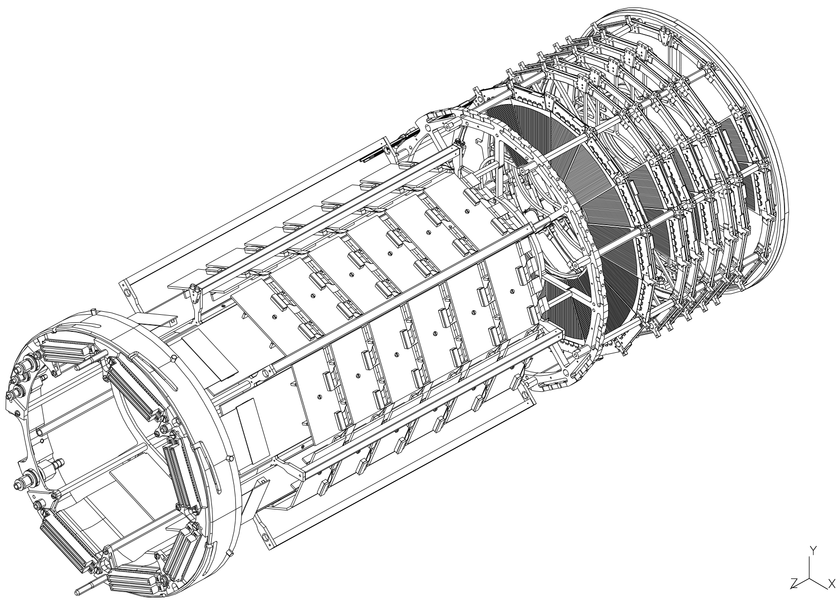

Figure 3.7: Forward Silicon Tracker global view.

The resolution displayed in Fig. 3.6 was obtained for subsample of electron candidates. The electrons had to carry an energy higher than 10 GeV deposited in SPACAL. They had to pass at least three planes of the BST1 or BST2. It corresponds to the electron tracks of a curvature less than $0.126\,\mathrm{m}^{-1}$. To obtain precise coordinates of hits the detector must have been aligned before.

The resolution of the detector modules will have a huge impact on the reconstruction of kinematical variables.

3.3 The Forward Silicon Tracker (FST)

The Forward Silicon Tracker (FST) is designed to measure particle tracks in the forward region of the H1 detector.

3.3.1 FST Layout

The Forward Silicon Tracker will be placed in the available space in front of the CST between the beam pipe and the central inner proportional chamber.

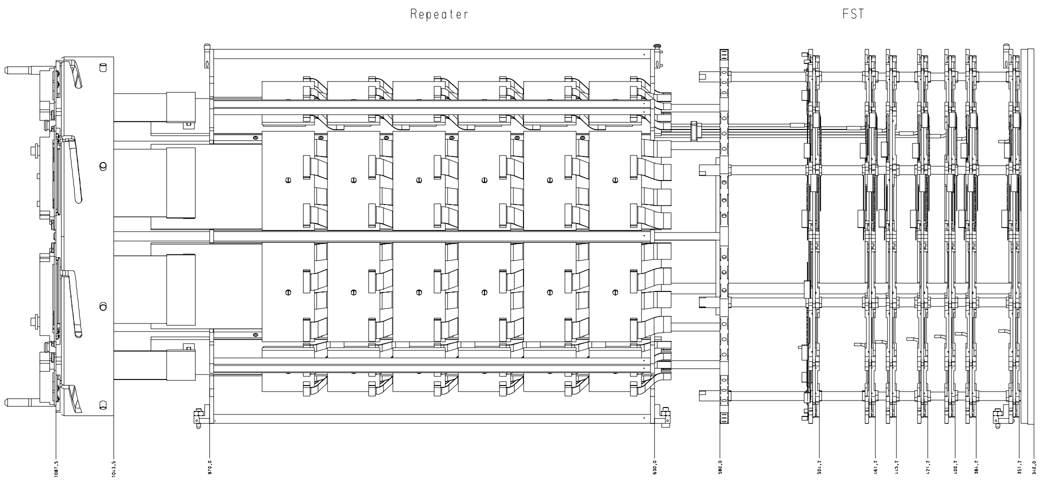

Figure 3.8: FST $r-z$ view

The FST will be built with the same hardware components as the BST since their structure is basically mirrored.

It will consist of five wheels equipped with the trapezoidal shaped ϕ–detector modules mounted back-to-back and of two additional planes with r–strip detector modules to avoid ambiguities during reconstruction.

The z–positions of the wheels and the types of their detector modules is shown in table 3.2. The $r-z$ view of the detector is shown in Fig. 3.8. Each

z − position mm	**Detector types**
351.2	u v
384.2	u v
400.2	r
421.2	u v
445.2	r
461.2	u v
504.2	u v

Table 3.2: Distances of FST wheels from vertex.

wheel consists of 8 sectors with two detector modules on each side. The FST has also two empty sectors (like BST3). The detector modules overlaps (as in the BST). To define the ϕ strip detector orientation (to or back to vertex) the detectors are called either u–strip or v–strip detectors depending on the orientation of their front side. The u–strip detectors face the vertex and they are mounted on the wheel side close to the vertex whereas the v–strips face the readout electronics and are mounted on the opposite side of the wheels. Strips of the u–detectors are crossing the strips of the v–detectors under an angle of 22.5° in the x–y–plane which allows a complete spatial reconstruction of a charged particle track.

The readout of the FST uses the same hardware as the BST.

The FST has the length of 75 cm it will cover the θ angular region from 6.7° to 18.8°. The inner and outer active radii are determined by the detector modules' active areas, which are the same as for the BST.

3.4 BST and FST physics goals

The FST will measure DIS electrons of very large y and Q^2 in the forward region. It will improve the precision of the vertex reconstruction. It allows to measure events where the neutral current cross section receives an important contribution from the structure function F_3. The measurement of F_3 requires a higher luminosity and a precise determination of the lepton charge asymmetry.

The BST will measure the electron of low Q^2 in the backward region where there is no any other tracking detector (see Fig. 3.3). The transversal momentum resolution was estimated to ($\delta p_T/p_T^2 \simeq 4\%$) if tracks are combined with the interaction vertex or if they are linked with CJC tracks only. A single track resolution of about 130 μm can be reached.

Both detectors will extend the acceptance of H1 detector for charm physics (see Fig. 3.9). Monte Carlo studies has shown that the BST3 enable to increase the detection of the D^* decays at low x and the FST at high x [22]. Assuming the FST detector modules resolution of 20 μm transversal momentum resolution $\delta p_T/p_T^2 \simeq 4\%$ can be achieved if FST tracks are linked to the interaction vertex. This resolution improves approximately twice, independently of the vertex, if FST and FTD tracks are combined.

The charm structure function F_2^c will be measured precisely and with higher statistics due the maximum coverage of x range. The BST will also extend the measurement of the gluon distribution function with charm and beauty quarks at low x by $1-2$ orders of magnitude [22].

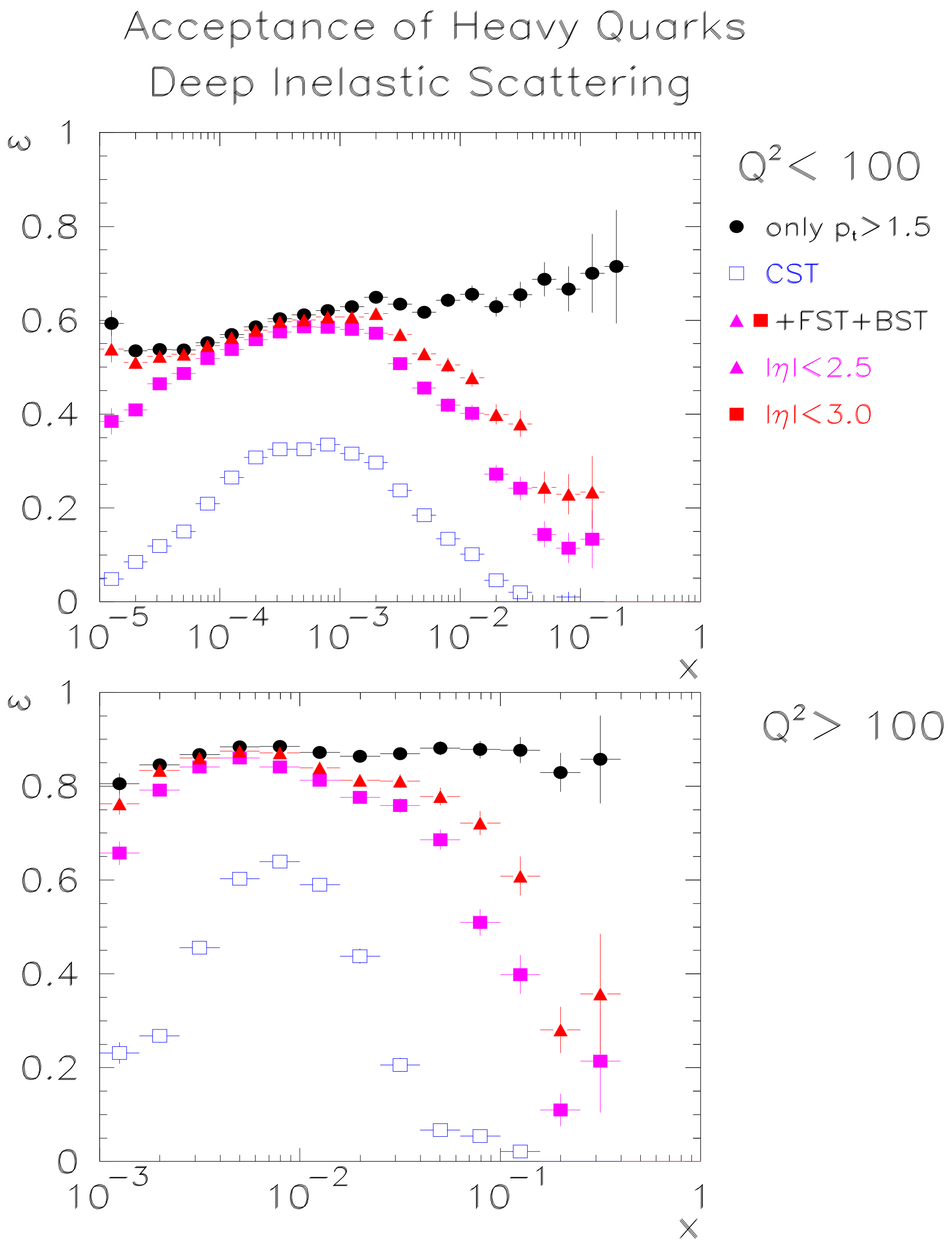

Figure 3.9: Acceptance for D^* decays using the CST and after adding BST and FST with different assumptions on the acceptance range of η [22].

Chapter 4

FST and BST Detector Modules

All three types of detector modules are described in detail in this chapter. In addition the measured properties of detector modules are presented here. Most of the tests which are currently in progress are of general use for every type except the laser test, which is done only for the strip detectors since the pad detectors need to be tested in a real particle beam. Moreover the pad detector is covered with an Al–layer which makes impossible to carry out the laser test.

All detector modules have the same trapezoidal shape and size shown in Fig. 4.1. The thickness of the n-type silicon bulk differs: $280\,\mu$m for ϕ–strip sensors, $300\,\mu$m for r–strip sensors and up to $380\,\mu$m for pad sensors. The technology of production of these sensors is basically similar for all types.

The p^+ active structures (strips, pads) are ion implanted on the front side of the n–type silicon bulk whereas the n^+ anode (back side) is made by high temperature diffusion. It covers the whole backplane, the surface of which is completely covered with an aluminium layer. All detectors are AC coupled with a thickness of the field oxide layer of about 200 nm (see Fig. 4.2). The coupling capacitance between the aluminium and a silicon structure of the width $10\,\mu$m varies from 10 to 15 pF/cm. The pad AC capacitance is about 3.3 nF.

All the sensors have a guard structure surrounding the bias ring to avoid a distortion of the electric field at sensor edges.

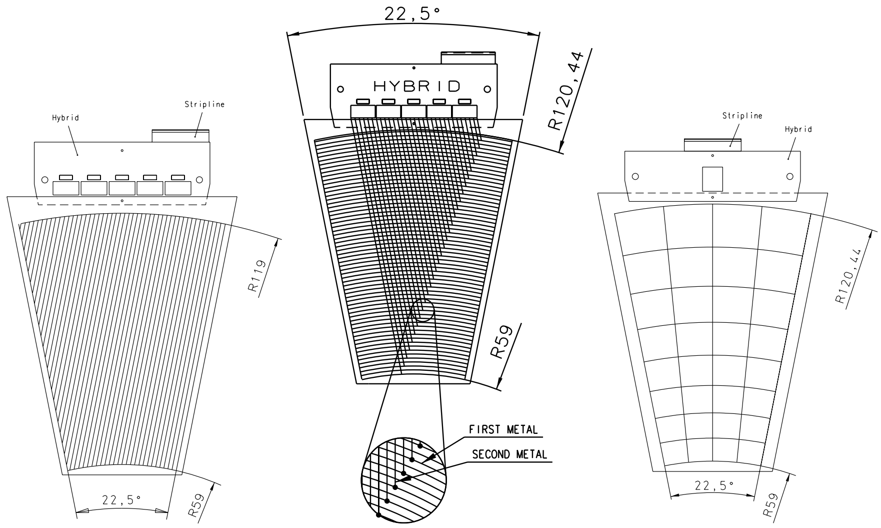

Figure 4.1: Schematic view of the detector modules with depicted hybrids. From left: ϕ detector module; r detector module with schematic view of the double metal contact strips; pad detector module.

4.1 ϕ sensors

The ϕ–strip sensors were designed by DESY–IFH Zeuthen. MPI Munich developed their production masks which were then written at Siemens. The production of sensors has been made by CIS Erfurt.

The p^+ strips are in parallel with one of the edges of the detector module. The end of the strips is limited by the outer (inner) radius of 119.9 mm (59.0 mm) and by the right edge of the detector. Borders between the active area and the right and left edge of the detector module are 1.5 mm wide.

Every third strip is read out (see Fig. 4.2b). The distances between the 640 readout strips are 75 μm. Two additional intermediate strips are between two readout strips to obtain a better defined charge division and therefore higher spatial resolution of the detectors. Thus the distance between neighbouring strips is 25 μm.

Contact to the readout elements is provided by small readout pads at the top edge of the sensor which are gathered into five groups of 128 pads at the top of the sensor. Each group has two rows of readout pads.

Two larger contact pads for the bias voltage and the guard ring are in the upper corners of the sensor. The p^+ area connected to the bias voltage leads

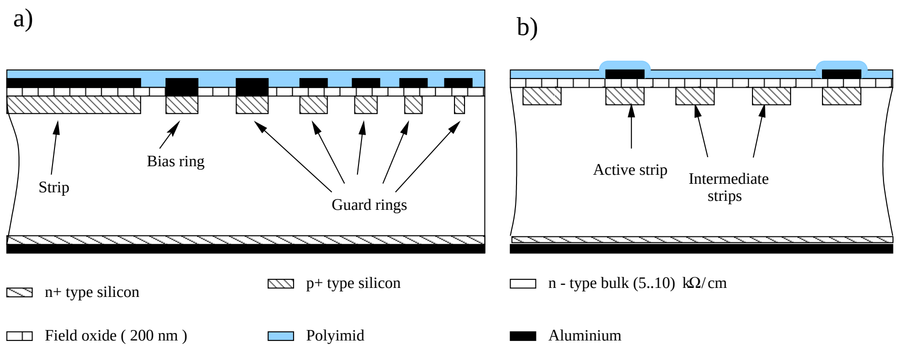

Figure 4.2: Cross section through the ϕ wafer a) in strip direction b) perpendicular to the strip direction

around the whole active area. All strips need a sink for the leakage current. Therefore they are connected via the so called "punch–through" transistor to the bias structure. This "punch–through" is made by a special design of the strip corner: A gap between the p^+ strip and the p^+ bias structure consist of n–material (bulk) thus forming a n–channel FET operated in pinch off mode.

The inner widest guard ring is also connected by "punch through" to the bias. We connect it to ground separately to be able to measure the guard current. The outer guard rings are without a direct contact to the ground. They function like field effect transistors in series with a punch through effect similar to the bias voltage (see Fig. 4.2).

4.2 r sensors

These sensors were made by MICRON Semiconductor Ltd. They are double metal AC coupled strip detectors.

The p^+ doped active area consists of arc shaped strips with an increasing radius from 59.0 mm up to 120.44 mm with a step of 48 μm. On top of the strips there is an isolation layer of 0.2 μm field oxide (AC coupling) covered with aluminium strips (called the first metal layer). The contact to the readout pad in the upper part of the sensor is provided by a second metal layer. The contacts between aluminium strips of the first and of the second metal are 4 μm (thickness of the dielectric layer) deep metalized via holes.

The bias and the guard ring are designed differently compared to the ϕ sensors. The bias voltage is connected on the left side to each odd strip

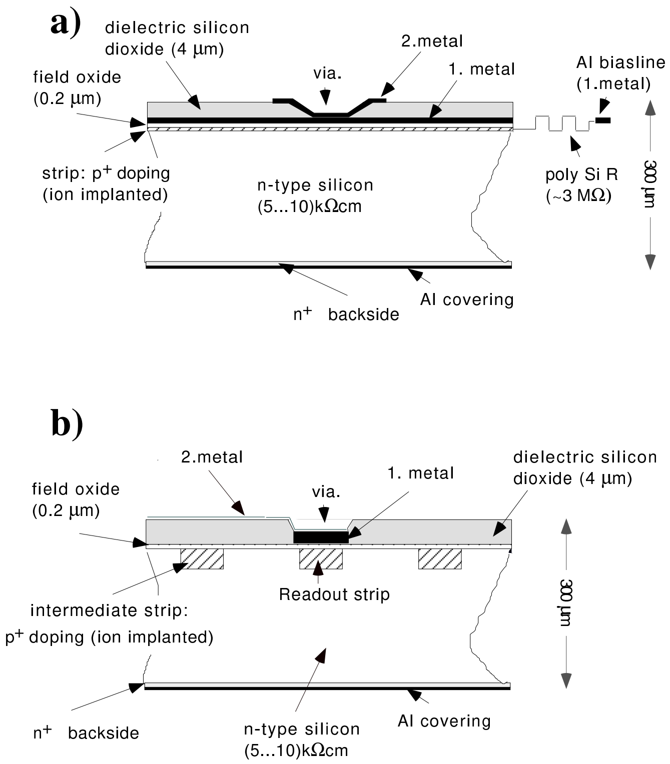

Figure 4.3: Cross section through the r wafer a) in horizontal direction b) in vertical direction

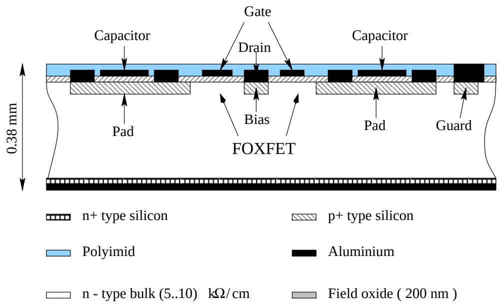

Figure 4.4: Cross section through the pad wafer in horizontal direction.

(intermediate) and on the right side to each even strip (readout strips) by means of polysilicon resistors which are individual for each strip. The guard structure is very simple and consists of one p^+ strip surrounding the active area with two aluminium contacts to the hybrid placed at the top of the sensor. The metal layers as well as the bias ring are schematically depicted in Fig. 4.3a,b.

The r–detectors have been used in the H1 detector since 1997. They will be implemented in the new BST and FST as well.

4.3 Pad Detectors

The pad detectors were also produced from MICRON Semiconductor Ltd., but their construction is different.

They have 4 p^+ doped pads in each of 8 rows with different radii (see Fig. 4.1). The area of the p^+ doped pads differs whereas the area of the AC coupling aluminium contacts is the same for all pads. The remaining area of the aluminium pad which does not compose the coupling capacitor is DC coupled and connected to the p^+ silicon.

The bias is designed using FOXFETs. One p^+ strip runs between two pad rows. It is contacted directly to the bias voltage contact in the right upper corner of the sensor. Each pad has a small "nose" pointing to this bias "rail". The gap between the "nose" and the bias "rail" is covered with the field oxide. On top of the gap there is an aluminium line which acts as gate electrode for the MOSFET built this way (see Fig. 4.4). By means of the gate the pinch off resistance of the FOXFET can be regulated. It is used for test purposes only. Under normal running conditions the gate is connected to the ground; this configuration is similar to the ϕ–strips sensors.

A guard ring surrounds all pads (active area) similar to the r–strip sensors.

4.4 Tests

All detector modules need to be tested to avoid any systematic loss of efficiency. The detectors have to be stable because they have to stay for a long time in the H1 detector biased without any direct access. One has indirect access by means of the slow control and by off–line analysis only.

4.4.1 Static tests

To test the properties of the sensors static tests are applied. Current/voltage (I/V) and capacitance/voltage (C/V) characteristics are measured either on the sensor directly or on its test structures (see Fig. 4.5).

- **Test structures**

All sensors are cut of a 4" silicon wafers (see Fig. 4.5). The remaining parts of wafer contain different test structures which are suitable for tests which could damage the sensor structure or for the measurement of specific properties of the sensor which cannot be measured directly on the sensor itself. The break through voltage of the coupling capacitors and the depletion voltage are measured on these structures.

Measurement of depletion voltage

The dependence of the junction capacitance on the bias voltage is measured on two elements situated on the test structures. The full depletion voltage of the sensor is then computed.

The small structures (see Fig. 4.5) are representing the properties of the sensor because they are processed on the same wafer simultaneously. The square of the p^+ doped area of the test structure is surrounded by one p^+ strip which corresponds to the guard ring of the detector. Two test structures are measured. They are marked Lvb and Svb in Fig. 4.5.

A manual prober is used to access the structures. One needle contacts the aluminium contact pad which is DC coupled to the p^+ doped silicon pad. This needle is used for the measurement of the capacitance of the structure.

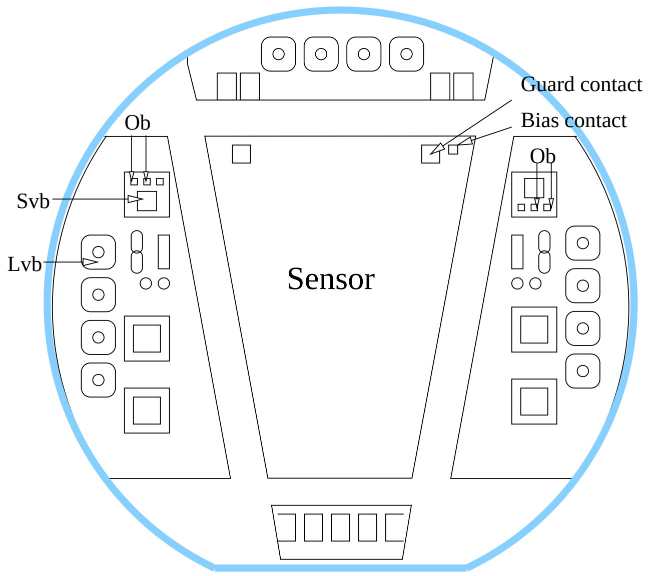

Figure 4.5: Schematically depicted the wafer with sensor and test structures.

The second needle is contacted to the guard ring. The backplane is connected to the positive potential V_{depl} of the voltage source. This voltage varies with respect to ground in small steps up to typically 100 V while the capacitance is measured. The depleted depth in the bulk grows with the square root of the bias voltage while the capacitance decreases according to the formula

$$C = \varepsilon_0 \cdot \varepsilon_R \frac{A}{d} \tag{4.1}$$

where A denotes the area of the capacitor (test structure), d means the distance between its planes (the depth) and ε_0 and ε_R are the permittivity of vacuum and relative permittivity of the material.

The dependence of the capacitance C on the bias voltage V for a not fully depleted detector can be obtained from the relation for the depth of the depleted volume (3.1) and the equation (4.1)

$$C = \frac{\eta}{\sqrt{V}} \tag{4.2}$$

where the constant η includes the properties of the silicon, the geometry of the test structure and the densities of dopants. The contact potential is neglected compared to the bias voltage.

The equation 4.2 is valid only till the detector starts to be fully depleted. The dependence of the capacitance on the bias voltage changes and starts to saturate at a constant value. The voltage corresponding to this point is called depletion voltage.

The depletion voltage have been determined by three methods (see Fig. 4.6)

1. The extrapolation of the two linear parts in the "double–log" curve gives a virtual cross point which determines the depletion voltage.

2. The second method is based on the shape of the first derivative ($\frac{d \ln C}{d \ln V}$) (see Fig. 4.6b). The shape of the curve is approximately symmetrical around a certain point. The average of ($\frac{d \ln C}{d \ln V}$) is calculated. This algorithm is repeated until the used data set is symmetrical around this average. Then the depletion voltage corresponding this average is calculated backwards. The derivative in a certain point is calculated from the slopes to its neighbouring points.

3. A Gaussian fit to the second derivative of the capacitance spectrum (see Fig. 4.6c) is made. The mean value of this fit corresponds to the natural logarithm of the depletion voltage.

All methods gives very similar results although the first method gives systematically a smaller value by 1.5 V then the others. The accuracy is sufficient for our purposes. Due to the sensitivity of the derivative to fluctuations the most often used method is the first one.

Measurements and calculations are done automatically by a program written in Labview [20] on a Macintosh computer. The voltage source and capacitance measuring instruments are driven by this program via GPIB.

The full depletion voltages for the ϕ–strip sensors are in the range of 55 V to 75 V, for r–strip sensors the values are smaller: from 14 V up to 35 V. For the pad detector they are in the range of 40 V.

The results of this measurement are important for the operation of the assembled detector modules. The sensors should be operated at a voltage as low as possible (leakage current, stability) and as high as necessary (fully depleted detectors).

Measurements of field oxide break through voltage

The homogeneity of the thickness of the field oxide layer and its continuity determine the properties of the coupling capacitance of the strips.

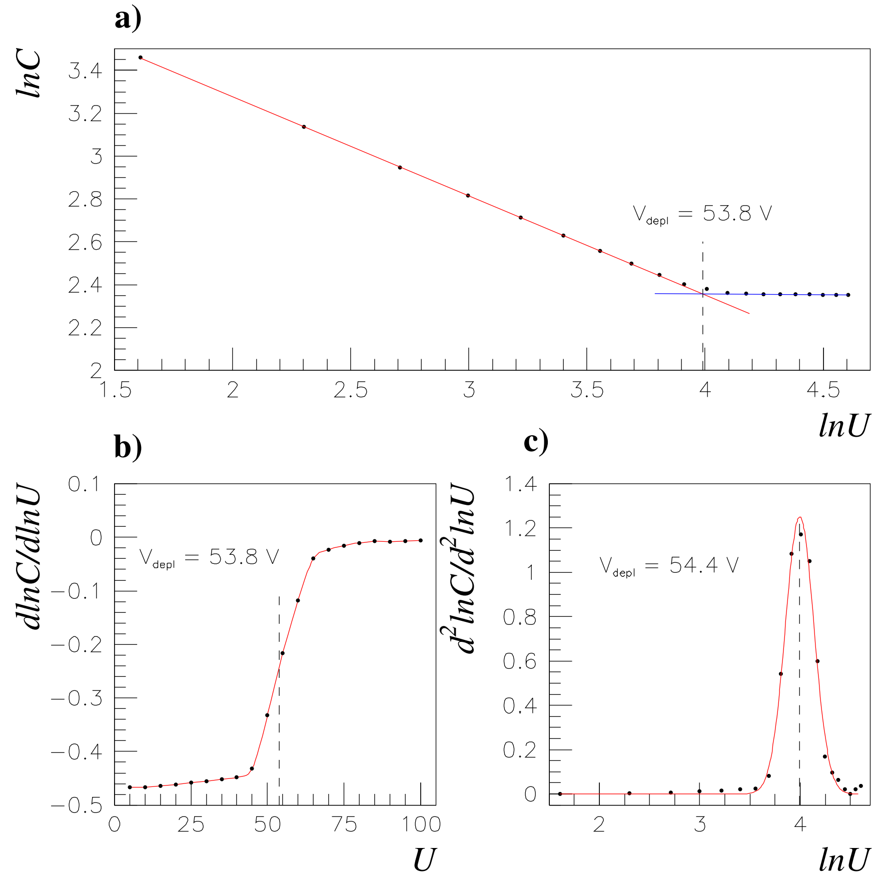

Figure 4.6: Dependence of the measured capacitance on the bias voltage. The depletion voltage is given a) by the intercept of two linear fits; b) by the center of symmetry of the first derivative; c) by the mean value obtained in the Gaussian fit to the second derivative.

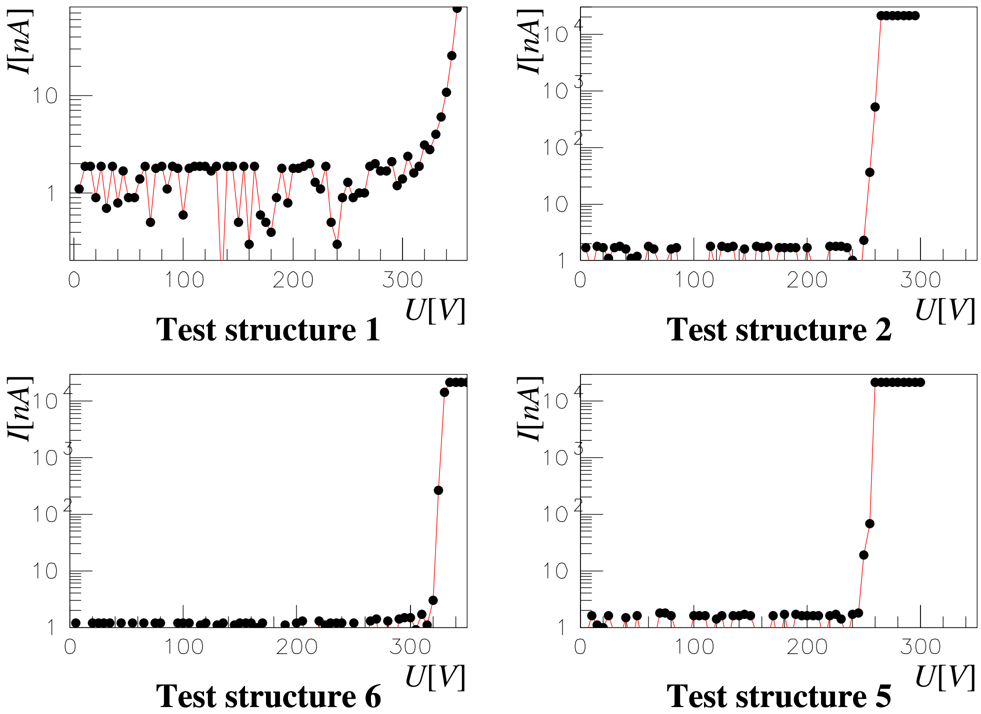

Figure 4.7: Examples of the field oxide break through tests.

The thickness of this layer is measured indirectly. This test is not done for all sensors but at least once for every production lot.

Again, the measurements are done on a manual prober. Two needles are contacted to the test structures which are signed Ob in Fig. 4.5. One needle is contacted onto the aluminium pad (AC coupled through the field oxide with the p^+ pad below). The second needle is contacted onto an aluminium strip leading to the p^+ strip surrounding the pad. A positive voltage is connected to the backplane, the negative pole is connected to the first needle. The current between these two needles is measured.

If a coupling capacitor breaks the current rapidly increases. Before the break it is stable and very small (see Fig. 4.7). The point where the current starts to rise corresponds to the field oxide break through voltage. It is proportional to the thickness of the field oxide layer. The break through voltage must be higher then the bias voltage used for the depletion of the detector under running conditions to avoid the damage of the readout chips in the case of a high current between the strips (pads) and the backplane (avalanche type ionization).

If the coupling capacitor is broken at lower voltages the field oxide is either too thin or not homogeneous. This kind of defects has been found for several sensors only.

- **Longterm (LT) tests of sensors**

The sensors have to stay for a long time at full depletion in the H1 detector. The test of sensor stabilities were made in special light tight boxes with BNC connectors outside. The contacts were bonded to the guard and bias contact pads on the detector (see Fig. 4.5). The sensor was kept in darkness for at least ten days under full depletion voltage +20%.

The currents of the guard and the bias were measured every day. Both currents have to be stable and below the specified limit of $3\,\mu$A. Examples of a good sensor with stable currents over the whole period of 12 days as well as a sensor with currents which are either unstable or above the limit are shown in Fig. 4.8. The current instability is caused by impurities in the silicon bulk or by surface effects. The test showed that the current stability depend on the production lot. In some cases only few sensors passed checks.

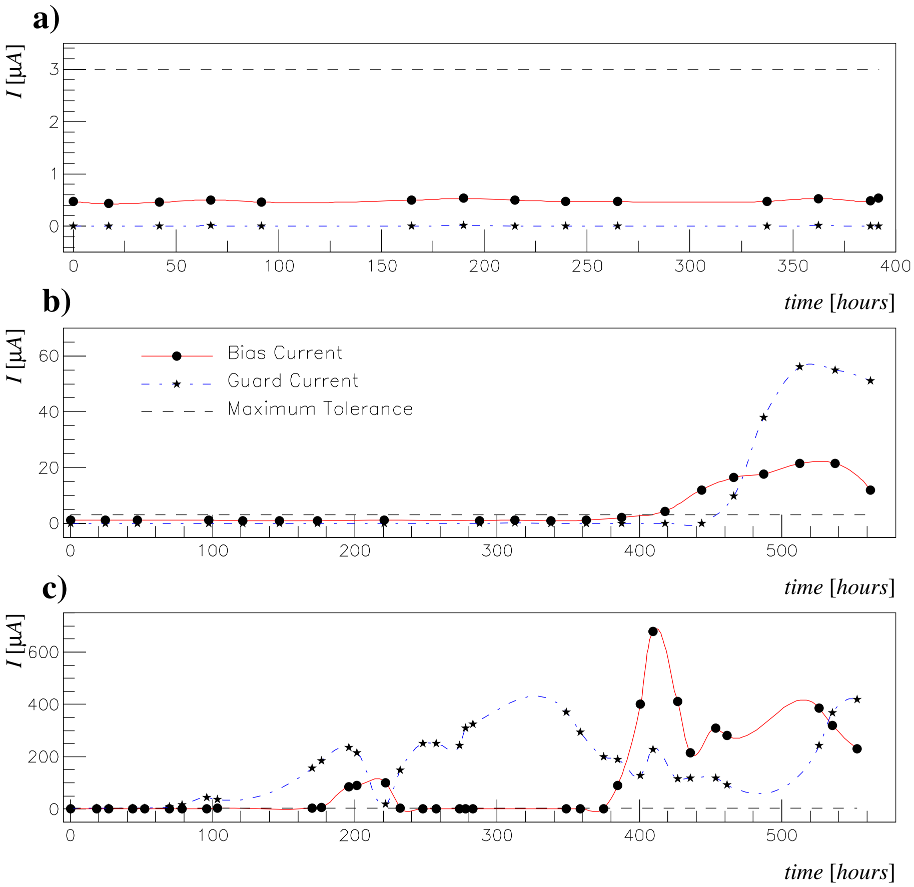

Figure 4.8: Examples of results of long term. a) The currents were stable over the whole period. b) The currents fluctuate too much and the current exceeds the tolerated value. c) The currents are increasing with time and exceed the tolerable value.

• **Voltage/current characteristics**

The sensor is made of high resistivity n–silicon. The silicon lattice may have failures or unwanted impurities which normally change the conductivity and the internal electric field. The I/V curve was measured for each sensor before the LT–test. It was repeated after the longterm test to check the influence of the LT. The currents were measured up to very high voltages of more than 300 V to find the voltage current characteristics and the break through voltage.

The measurement of the voltage/current characteristics of the bias and the guard ring in the boxes was done in the same way, without using the manual prober. The results of a good sensor are shown in Fig. 4.9.

As long as the detector is not depleted the bias current increases accordingly to Ohm's law because the resistance increases with the square root of the bias voltage. After full depletion it saturates at a certain value. Only the leakage current flows. The current rapidly increases if the bias potential reaches the break through voltage of the sensor.

The guard current also behaves as a *pn* junction but the break through voltage is normally not reached.

4.4.2 Dynamic tests

To test the quality of the detector in detail two dynamic tests are done for every strip detector module. On the sensor level the capacitance of each strip or pad, respectively, is measured. This test is called the **Strip test**.

The **Laser test** is the final check of the functionality of detector modules i. e. the sensors and the hybrids. (The readout elements will be described in chapter 5.)

• **Strip test**

The capacitances of the coupling capacitors of the r–strip sensor were measured directly by MICRON. The results were delivered together with the sensors. Since CIS Erfurt was not able to perform a strip test of the ϕ–strip sensors and manual measurement of all 640 coupling capacitors takes much time and is too difficult a specific setup and the corresponding software for it were developed to provide an automatic measurement.
Setup:

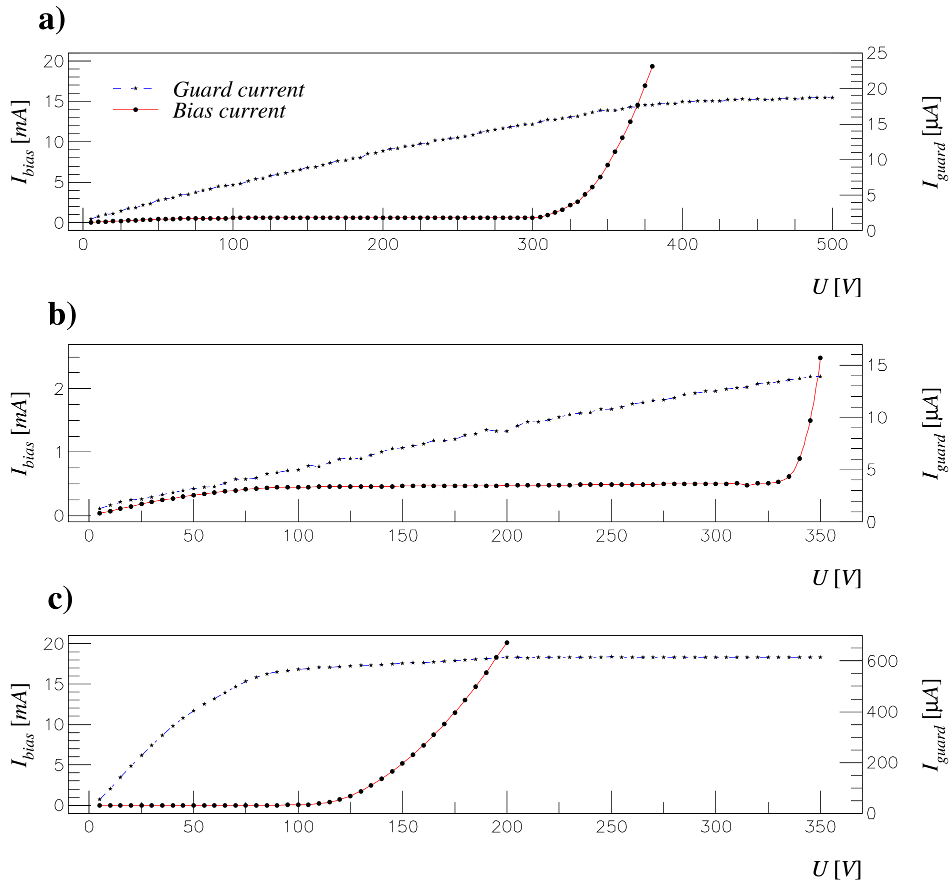

Figure 4.9: Voltage/current characteristics of a good sensor: a) Several days before the long term test with a manual prober. b) Before the long term test in the test box c) After the long term test in the test box

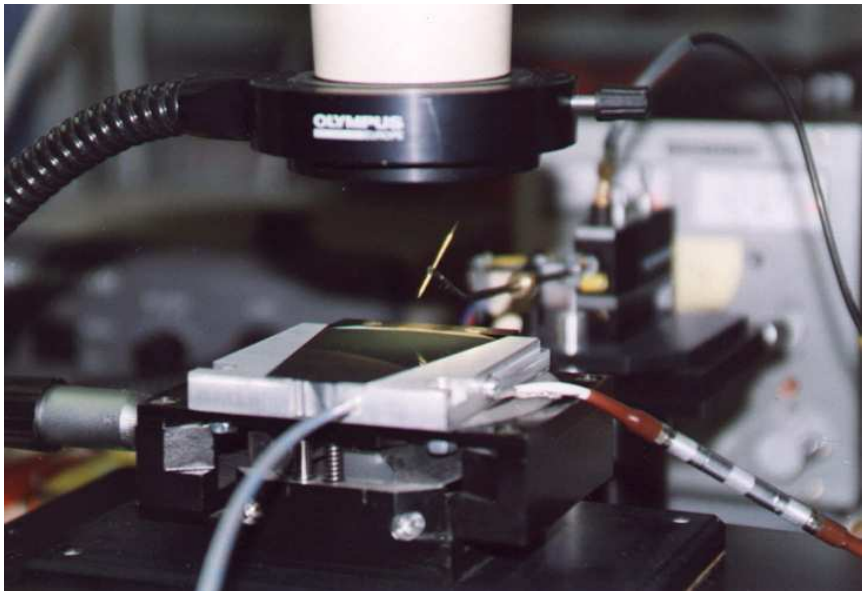

Figure 4.10: Snapshot of the strip–test setup, where the components are visible.

The readout bond pads of the strips have a size of 58x180 μm^2. The center distance (pitch) between two neighboring odd (or even) pads is 38 μm, the horizontal distance between even and odd pad rows is 130 μm. The pads are divided into halves with a very short neck. The lower part serves for the test. The upper part will be used for the wire bonding to the readout chip APC128.

The probe needle mounted at the tip of the lever arm makes a contact to the bond pads (to measure their capacitance). The lever arm contains a shielded cable connected to the capacitance meter. A support carries the socket together with the magnet coil and the damper.

The magnet coil enables lifting the probe needle with the lever arm. The mechanical coupling between the magnet and the lever arm has to be soft. Therefore a peace of foam coated with tape is glued to the magnet lever making a smooth surface. The lifting force of the magnet can be adjusted with a small spring by adopting its length. To avoid oscillations of the needle caused by the kick of the magnet the lever arm has to be adjusted carefully.

The damper is used to slow down the sinking of the lever arm. The sinking speed can be set with an movable small weight on the lever arm.

The damper consists of a small tube closed on one side and a piston on a small stick fixed to the lever arm. The damper stick has to be in vertical position when the needle is contacting the pad. This position has to be found using the lever arm's holder.

The tested sensor is vacuum fixed on the XY–table. The second contact of the capacitance–meter is connected to the backplane of the sensor. A bias voltage of $-30\,\mathrm{V}$ is connected to the backplane of the detector. This way the sensor's bulk is conducting and the coupling capacitance is measured only. A snapshot of the setup is shown in Fig. 4.10.

The XY–table is driven by a Macintosh computer using the modem port which is connected to the XY–table controller. This device assures monitoring and driving of the XY–table. It is controlled by string commands of the computer.

An electronic circuit was designed to drive the magnet. It provides the current for the magnet coil after receiving a TTL–level signal[1] from a digital I/O card (PCI DIO 96 card in the Macintosh computer). For reasons of safety the lever arm should stay in the "up" position if the current is switched off. The capacitance–meter is read out with the Macintosh using the GPIB interface.

The program written in Labview 5.1 [20] (graphical programming tool) was developed in the framework of this thesis. The measuring process as well as the analysis and data storage are driven using this program. A short part of this program is shown in the appendix A (the full length of the program is about 50 pages).

Measurement:

It consists of four phases:

1. *Initialization* where all devices and values are set to the default values. The capacitance is measured using a frequency of $10\,\mathrm{kHz}$; the velocity of the XY–table is set to a value of $0.25\,\mathrm{mm \cdot s^{-1}}$.

2. *Calibration* is needed to know the precise positions of the (vacuum fixed) sensor which is obtained from the measurement of the table coordinates when the needle is positioned over the first contact pad and over the 638^{th} pad (last contact pad in the upper row) on the sensor. The slope and the first position is obtained from a calculation using the

[1] Trigger signal consists of two bits which are then validated with the logical element on the circuit

calibrated values, the known distances between pads and pad groups. The calibration needs to be done under a microscope. Correct positions are validated by responding to queries of the program.

3. *Data taking* starts after the end of the calibration. All strip–capacitances are measured. If the measured value is not in a range from 10 pF up to 1 nF the contact between the needle and the pad was probably not reliable and the value is measured automatically a second time. This usually happens if the aluminium contact pad is covered with dirt or oxide more than usual and the needle does not contact the Al–surface.

4. *Checking of bad values* is done at the end of the measurement to make sure, that bad strips marked by the analysis after the automatic measurement were not found with the mentioned contact failure. Critical measurements (strips in doubt) may be repeated with a manual addressing by the operator. After the completion of the measurement the data are analyzed and stored on a disk.

Analysis:
The dependence of the strip capacitance is analyzed by the program mentioned above. The capacitances are proportional to the length of the strips. The dependence of the strip length on the strip number counting from zero from the shortest active strip is shown in Fig. 4.11a). The additional capacitance of the contact lines between the bond pads and the strips have to be taken into account. Therefore the length of these contacts (see Fig. 4.11b)) is added to the length of the strip (see Fig. 4.11c)). The real measurement of one detector module without any failures is shown for comparison in Fig. 4.11d).

The capacitance dependence on the length of the strips and lines[2] is very complicated and exhibits the sixfold structure. It contains square root terms, but for the analysis it is sufficient to use a polynomial fit of the second order separately for each of the six strip intervals (see Fig. 4.11c). The strip capacitances which differ more than one standard deviation from the mean of differences between the fit and the data plus a tolerance of 5 pF are excluded from the next fit. It is repeated while σ is higher than 0.3 pF or the number of iterations does not exceed 10. Then the relative errors are calculated and the strips with a relative error higher than 5% are marked as defective.

[2]As already mentioned: the readout lines are on top of p^+ strips, thus they also contribute to measured capacitance like the strips do

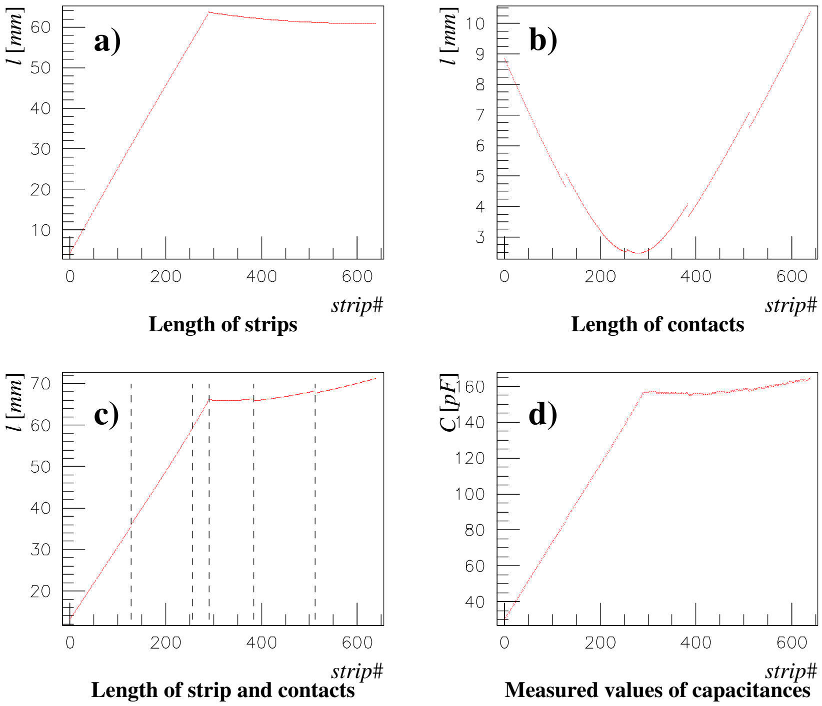

Figure 4.11: Lengths of strips and contacts in comparison with the measured capacitance.

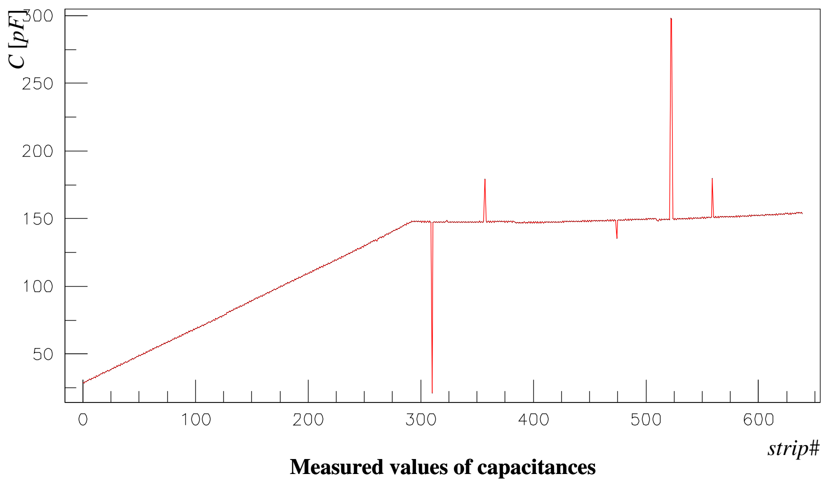

Figure 4.12: The example of the ϕ–strip module with defects

The possible defects are shown in Fig. 4.12. A shortcut between two strips causes a two times higher value of the capacitance for two neighbouring strips. It is usually caused by an aluminium bridge which was not etched correctly (lithographic failure). Such a defect can be easily seen on the detector. The lower capacitances are probably caused by a break of the aluminium or p^+ strip. Higher values of the measured capacitance without neighbouring defects are caused by a bad field oxide ply which is probably broken (shorted) or too thin.

Sensors with not more than 7 defective strips are accepted for use in the BST and FST. The sensors failed in one or more of the described tests are sent back to the manufacturer.

- **Laser test**

The response of the assembled detector module together with its readout elements is tested in this (final) test.

The test setup consists of a red–light semiconductor laser (685 nm), an optical system to focus the laser light onto a 25 μm spot, a current pulse generator, a pulse generator, an XY–table, readout and control components and a Macintosh computer. An Labview program were developed for the driving of all components the data analyses and hit finding.

The detector modules are fixed on the XY-table and the signal induced by the laser spot is read out and analyzed. Ten laser pulses are measured for every strip.

The mechanical position of the detector is adjusted in a calibration run similar to the calibration in the strip test. Signals from all strips are displayed on the screen during the calibration run. By shifting the table using a joystick the position of the strips are fixed. One observes the signal induced by the laser pulse at least on the first and the last strip. Than their positions are used for the calibration of the position of the detector module.

The next steps are basically similar to the strip test. The whole measurement is done automatically. Pedestals, noise and the efficiency of each strip are calculated using a hit finder during the measurement and are displayed and saved at the end of the laser test run.

Laser pulse

The laser pulse is generated after a trigger generated by the OnSiRoC module. This trigger is programmable with the sequencer code which drives the readout and the sampling of the signals (see the section 5.3). It is generated for each sampling phase of the analog pipeline chip (APC). An example of the sequencer code is given in the appendix B.

The trigger is passed to the pulse generator where a pulse length of 100 ns is adjusted as a gate for the current generator. The value of the laser current is set by a voltage controlled current source. A time scan of the laser pulse was done to find the optimal readout time slice (see Fig. 4.13). The scanned pulse consists of two parts, the pulse induced by the laser itself and the response of the electronics (integrating preamplifier in the APC). The optimal time slices are 4,5,6. Therefore the fifth time slice was chosen.

The light is focused with an optical system onto a spot of 25 μm on the sensor's surface. The laser signal is visible on four strips around the strip to which the light was focused.

Hit finder and calculations

A hit finder has to be included in the analysis of the signal to determine the efficiency of each strip. This finder had to be similar to the BST hit finder algorithm used in H1 to get compatible results.

64 events without any laser trigger are taken to calculate pedestals of each strip. The σ of the pedestal distribution is taken as the initial noise of that particular strip.

Ten laser events are taken for each strip and the sets of these spectra are then analyzed in the following way: The pedestals are subtracted from

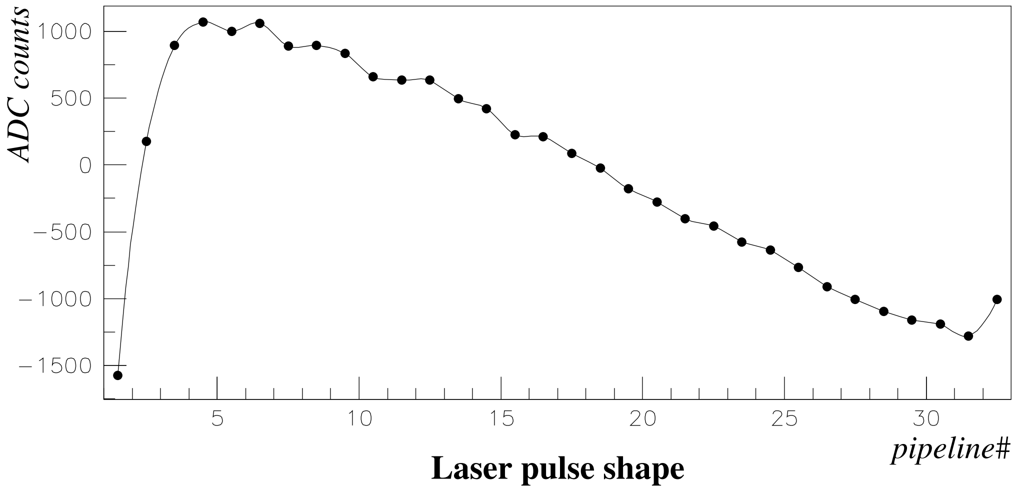

Figure 4.13: The scanned laser pulse response found in the capacitors of the APC analogue pipeline.

signal values. The mean over 128 channels corresponding to one APC is calculated. This value (the so called common mode) is subtracted from the pedestal corrected signal values after the to find the "pure" spectrum. Then the values which are higher than 3σ of the "pure" spectrum plus additional 100 ADC counts are marked as hits. The number of the hits divided by the number of laser pulses corresponds to the efficiency of the strip. An average height of the laser pulse signal for each strip is calculated in addition.

To obtain the current values of the pedestals and the noise fed into the next hit finder the weighted average of noise $\mathcal{N}_i$ and the pedestals $\mathcal{P}_i$ are calculated

$$\mathcal{N}_i = \frac{e^p \cdot \mathcal{N}_i^p + e^c \cdot \mathcal{N}_i^c}{e^p + e^c} \tag{4.3}$$

$$\mathcal{P}_i = \frac{e^p \cdot \mathcal{P}_i^p + e^c \cdot \mathcal{P}_i^c}{e^p + e^c} \tag{4.4}$$

where i denotes the channel (strip) number, $\mathcal{P}_i^p$ and $\mathcal{N}_i^p$ mean the pedestals and noise from the previous events, $\mathcal{P}_i^c$ and $\mathcal{N}_i^c$ are the pedestals and noise calculated from the currently taken e^c number of events (10), then e^p is the number of the previous events including the first 64 events for the initial values. The channel where the laser pulse is measured and its four neighbours

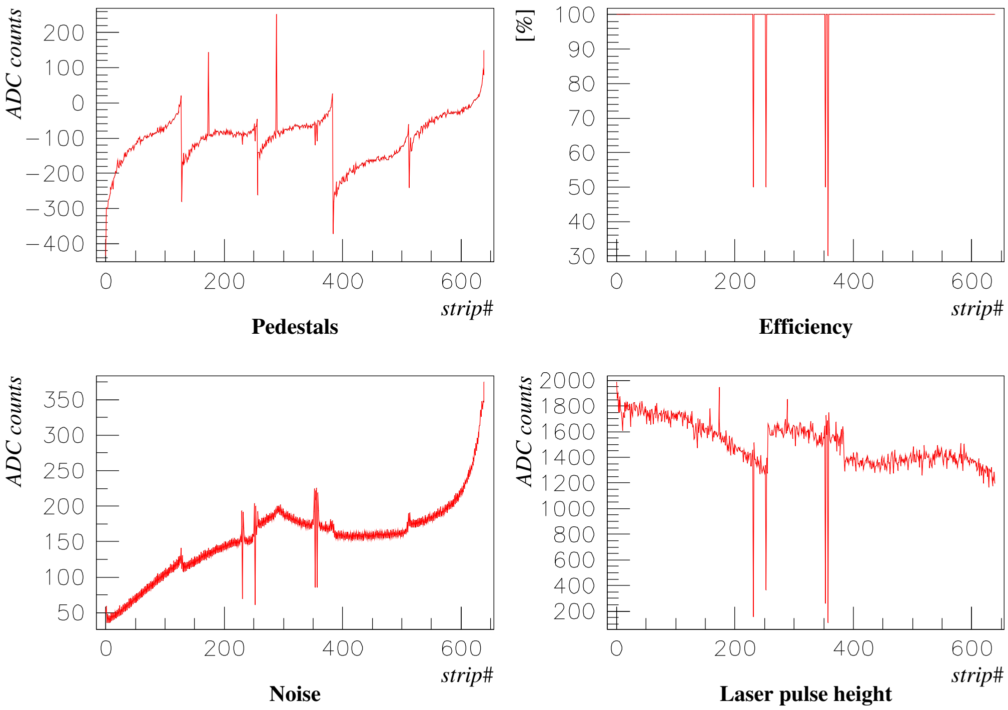

Figure 4.14: The results of one laser test.

are excluded from these calculations.

Results

An example of results from the measurement of detector modules is shown in Fig. 4.14. The distribution of pedestals exhibits a periodical structure which corresponds to the strip groups of the five tested APC. Deviations from a smooth approximation of ADC counts within each APC is caused by strips defects of which have been already found in the strip test.

Noisy strips are detected as the peaks in the noise spectra, the slopes of which correspond to the strip capacitors except the rise of the noise in the end part of the detector module. This effect was checked under H1 conditions but no such behavior was observed. Therefore this is caused by the laboratory setup. The reasons for this behaviour have not yet been found.

The dead and bad strips are determined inspecting the plots of the efficiency. which is the crucial parameter for determination of the quality of the detector module. The average laser pulse height is only a cross check for the efficiency.

These test have been performed for several modules only and series checks will continue in autumn this year.

Chapter 5

Readout and Control of FST and BST

The readout and control system of H1 silicon trackers is introduced in this chapter. Results of tests of the front–end electronics, namely APC chips and decoders are discussed. The readout system was firstly commissioned and operated in 1997 for the CST and the BST1 detectors.

5.1 Data Acquisition

The parameters of the H1 silicon detectors and the H1 environment put the following requirements on the readout system:

1. The large number of readout channels leads to the need of a highly integrated front end system where the signals are multiplexed prior to readout.

2. The low signal amplitudes ($\sim 20\,ke^-$) from silicon detectors make the preamplification in the closest position to the detector an ultimate necessity.

3. The HERA bunch crossing time is 96 ns and the delay of the first level trigger is approximately $2.5\,\mu$s. Therefore the storage of the signals in pipelines with a shift frequency of at least 10.4 MHz for a sufficient long time is needed.

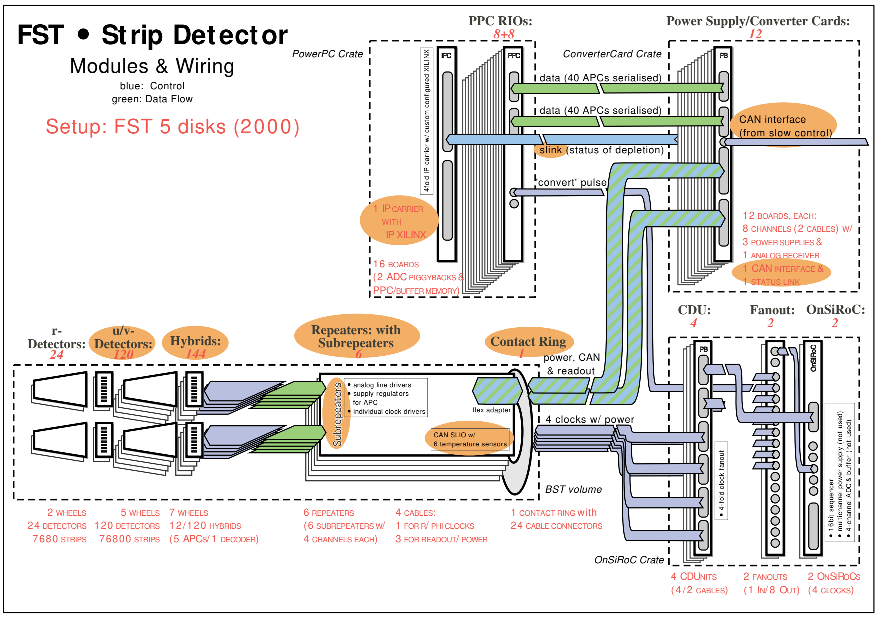

Figure 5.1: Proposed readout chain of the FST strip detectors with schematically depicted readout components

4. The front-end system has to be fast enough to avoid any additional contribution to the dead time of the whole H1 system when the detectors are being read out and thus insensitive.

5. A reduction of the raw data of silicon detectors is necessary before they are merged into the main data stream of H1 system because a huge number of strips are not hit and "empty". Therefore a reconstruction of hits is performed and only this information is then stored.

6. This information has to be read out and the system has to be prepared for the next data handling as soon as possible to avoid any second–order dead time in addition.

7. A certain flexibility of the system is required to allow for possible changes or addition of new parts.

The proposed solution of the readout chain is schematically shown in Fig. 5.1 which is a modification of the existing BST system.

The readout system consists of the following components:

The Power PC (PPC) : They perform the analog to digital conversion of data. The conversion is controlled with a clock signal (SQD). The CPU performs the online hit finding from 16 detectors. The PPC crate is linked to the H1 data logging with an optical fiber data transmission.

The Converter Card provides the supply voltages for the repeater boards and the detector hybrids. It includes the line receivers and level shifters for the detector output signals and transmits them to the PPC module.

The Patch Card distributes the clock signals from the OnSiRoC module to the repeater boards.

The OnSiRoC module is used to generate the clock pulses for the hybrids. It runs the sequencer code and will be described in detail later.

The Repeater (Motherboard) passes and distributes the supply voltages and clock signals to five subrepeater units connected to it. It also contains the slow control circuits for temperature monitoring.

The Subrepeater units contain the line receivers (clock and signal) and drivers for four detectors. They provide the distribution of power supply lines to the detector hybrids.

The Hybrid contains 5 APC128 readout chips and one or five decoder chips[1]

> **The Decoder chip** is used to convert the four clocks signals to parallel control signals of the APC128 chip. It will be described in detail in section 5.4.
>
> **The APC128 chip** amplifies and stores the signals from the detector in analogue pipelines (see section 5.3).

Some additional readout components are not shown in Fig. 5.1 (VMEtaxi controller card etc.).

The slow control system enable to monitor the operation of the detectors from the control room (temperature sensors, bias voltage sources and the radiation monitors).

[1]5 decoders are placed on the r–hybrid whereas only one decoder is used to drive all APCs on the new designed ϕ–hybrid.

5.2 The OnSiRoC Module

The **On**line **Si**licon **R**ead**o**ut **C**ontrol unit was developed especially for the control and the readout of the CST and BST. It has the capability to read out 4x2048 channels at sampling rates (pipeline) up to 10 MHz.

The OnSiRoC module can assure following functions;

1. readout and digitization of signals from detectors; not used for BST and FST;

2. delivery of all supply voltages to the Si–detectors and electronics; not used for BST and FST;

3. complete controlling and monitoring of the detector modules, namely transmission of the clocks and control signals to the APC chips.

The first two functions are applied for test purposes only, since:

- This module can not handle signals with significant common mode; hardware pedestal subtraction can be made only if the average pedestal is stable.

- The internal power supplies do not source the currents needed.

- The depletion voltage delivered by this module is not stable with no or with a small load.

To overcome these problems the functions 1 and 2 were included in other units i.e. PPC, Converter card and Patch cards.

Data acquisition is divided into the sampling phase and the readout phase. They have to be distinguished in the sequencer code with two trigger bits i.e. SQD13 which is generated before the sampling loop starts and SQD15 generated at the end of the readout phase. The sampling loop is interrupted using the external trigger signal (connected to one of the Lemo input signals (*COS Stop*) on the OnSiRoC front panel or the external trigger input at the modules backplane.

The OnSiRoC module is operated via VME interface by two 16 bit control registers and one 7 bit status register are.

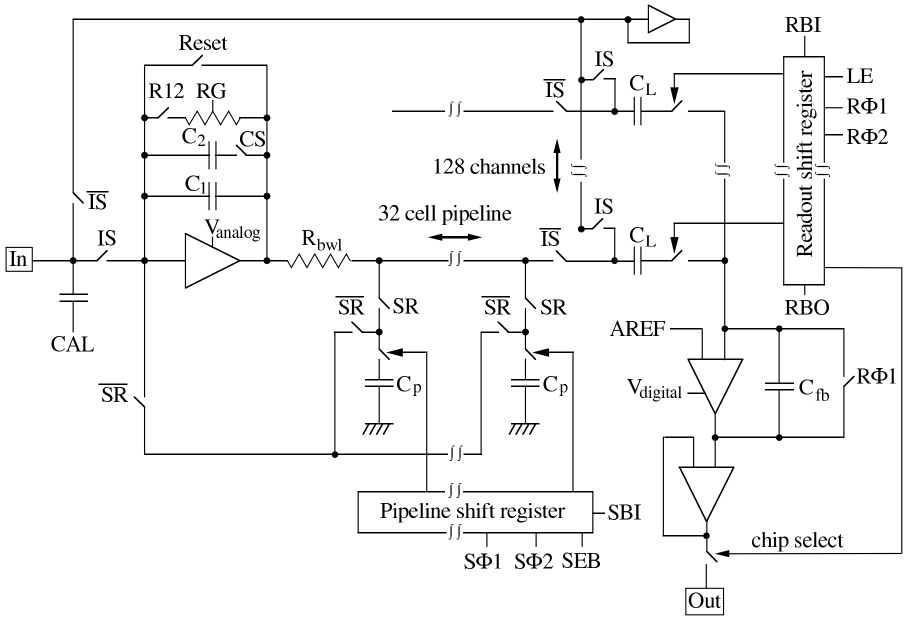

Figure 5.2: Circuit diagram of one channel of APC128

5.3 APC128 - readout chip

The APC128 chip was designed in SACMOS 1 technique for the H1 silicon trackers readout. It contains 128 preamplifiers, followed by a 32 time slices deep pipeline for the storage of the analogue amplitudes. The schematic diagram of one channel is shown in Fig. 5.2.

Each readout strip is connected to one input of the chip. The signal is amplified by the **Analog preamplifier** and stored to one of the 32 time slices of the capacitor array controlled by the **Pipeline shift register**. The signal from the addressed $\mathbf{C_p}$ capacitors is read out after a trigger decision and it is stored on the latch capacitor ($\mathbf{C_L}$). Then after addressing by the readout shift register the signal is again amplified by the output amplifier and passed to the subrepeater board. The APC is basically a switched capacitor network. Its functionality is ensuring by the control signals.

5.3.1 The Readout Procedure with the APC128

The whole readout procedure can be divided into four phases:

Initialization – resetting all the samples capacitors C_p and setting the latch capacitors to the initial value.

Sample phase – sampling of the input charge and storing the corresponding voltage into the capacitor array until this cycling is stopped by the H1 trigger decision.

Re–read phase – re–reading and amplifying the signals from the "signal" capacitor and storing the information on the latch capacitor.

Readout phase – readout of signals stored on the latch capacitors, amplification and conversion to a digital signal.

Initialization

All latch and sample capacitors as well as the preamplifier are reset in this phase.

Reset is switched on firstly and then by so called "race-through" of the **SΦ** clocks, it means that both clocks and **SBI** (set to the desired value) are active in one moment, **Pipeline shift register**, sample capacitors and the input preamplifier are reset.

Then the clocks are switched from **SΦ** to **RΦ** while leaving the **Reset** switch closed using the "race through" for the readout shift register (RBI=1). Thus all latch capacitors are set to the initial value. The latch capacitors are supplied with a stable voltage by the amplifier in the right upper part of the APC128 schematic diagram (see Fig. 5.2). Every clock "race-through" is done several times to be sure that each capacitor is erased (set).

The sample phase can start after this procedure.

Sample phase

The switch **Reset** is opened at the beginning of this phase. Otherwise all signals would be lost.

IS and **SR** switches must be closed during the whole sample phase. The **R12** switch is closed in order to integrate the signal charge from the detector with the preamplifier.

SBI is set to logical one and shifted through the whole **Pipeline shift register** using the **SΦ** clocks, thus addressing the sample capacitors in one row. A new **SBI** bit is generated after one cycle of the register. The information stored in the pipeline capacitors is then overwritten. This procedure is repeated in a loop.

The appearance of the H1 trigger stops the sampling.

Re–read phase

The first step is the opening of switches **IS** and **SR** to disconnect the detector from the chip in this phase. **R12** is opened at the same moment to switch the preamplifier to a higher gain. These switches will be kept in this stage until the end of readout.

The **Reset** is switched on after disconnecting of the pipeline register using the **SEB** bit. The output amplifier and the **Readout shift register** are reset by the "race through" of the **RΦ** clocks while RBI is active. While the capacitors are still disconnected the pipeline shift register is clocked to the intended position using the clocks with the generation of an overflow signal, which means that if the end of the shift register is reached the **SBI** bit is generated once more for the next clocking. Thus the capacitor containing the strip signal is addressed.

The **Reset** is then opened and using the **SEB** bit the charge stored on the addressed sample capacitor is re–read, amplified, the polarity is once more inverted and stored on the latch capacitor. This can be done for an arbitrary number of sample capacitors, their signal charge is then added to the already stored charge.

Readout phase

The stored charge is read out serially from the latch capacitors by clocking the readout shift register (**RΦ** clocks) and then amplified with the readout amplifier.

The contact to the **Readout shift register** is enabled with the bit **LE**. Then the **RBI** bit is shifted through the **Readout shift register** to connect latch capacitors sequentially. The **RBI** bit is passed to the next APC through an **RBO** after reading out the current APC. The sampling loop is restarted at the end of a readout phase to wait for the next data taking.

An example of such a cycle is shown in Fig. 5.3. Apart from the sample phase the other phases are limited in time. Due to this fact the initialization can be placed at the end of the readout phase.

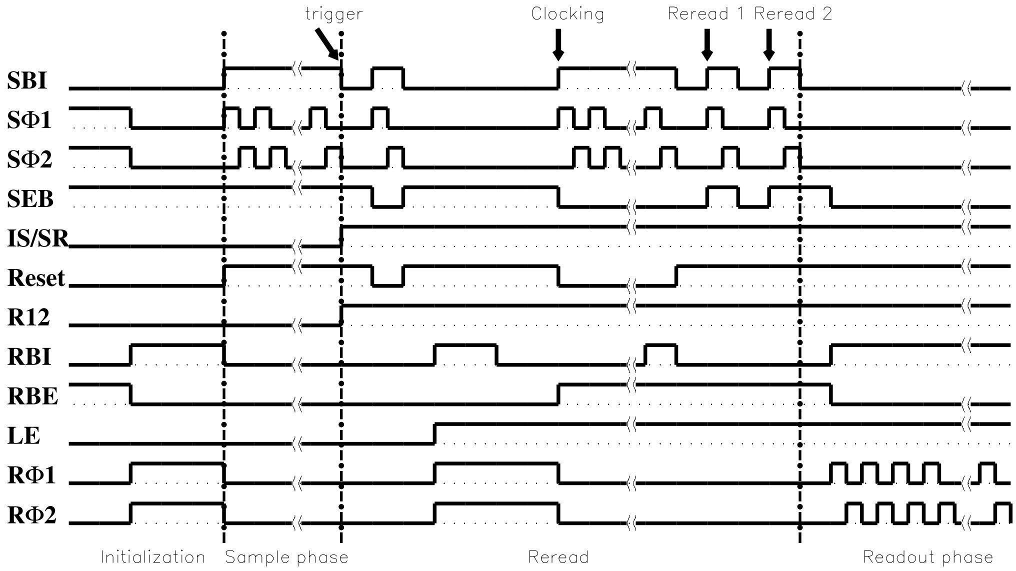

Figure 5.3: Sequence of control signals for operating APC128.

Relaxation times to discharge the capacitors and reset the amplifiers have to be taken into account.

5.3.2 Tests of the APC128 chip

All APC128 chips were delivered from the manufacturer without being tested. Therefore they are tested to avoid any losses of the detector efficiency. For the BST and FST strip detectors a total number of 1700 good chips is needed (including spare chips).

Test setup

Test setup consists of the following parts:

- mechanical parts:
  - Magazine for up to twelve APC128 chips
  - Microscope with XY–table and probe fixture
  - Probe card with contact needles

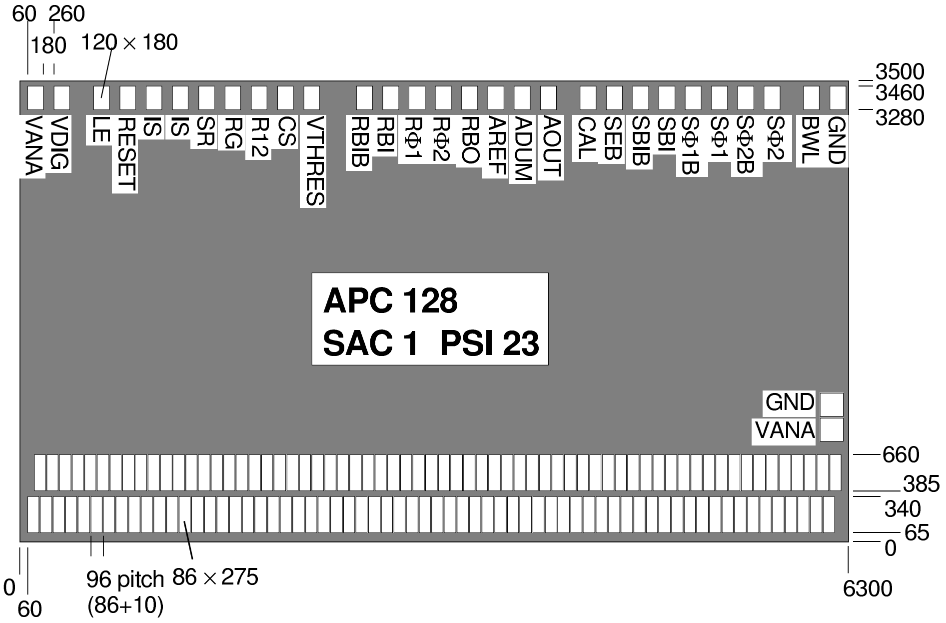

Figure 5.4: APC128 bond pad layout. Units depicted in the Fig. are in μm.

- electronics:
  - Fanout (glued to the hybrid)
  - Modified hybrid with one decoder chip
  - Subrepeater
  - Repeater motherboard
- control units:
  - OnSiRoC module
  - VME controller card
  - Oscilloscope
  - Macintosh computer with the VME interface.

The chips are fixed with vacuum in the magazine which is mounted on the XY–table and fixed there with vacuum too. The contact from the APC chip's bond pads to the hybrid is provided by small needles on the probe card. The adjustment of the contacts has to be done under the microscope because

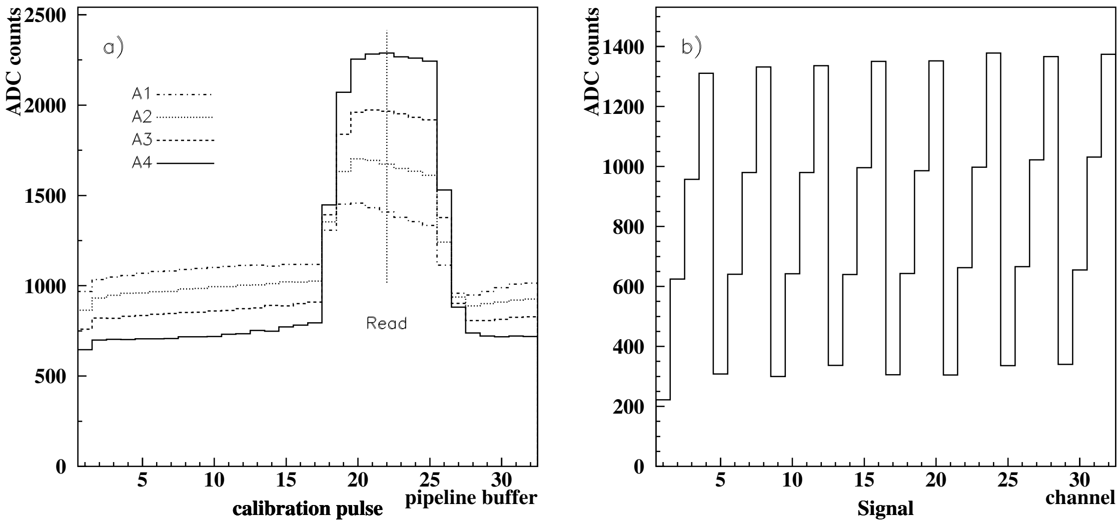

Figure 5.5: The calibration pulse of APC a) along the time slices. Four kinds of amplitudes are shown. The $22^n d$ time slice is read out. An offset voltage was used to shift the amplitudes up. b) Calibration pulses vs. channel number like were visible on the oscilloscope.

of the small size of the APC contact pads (see Fig. 5.4). The cables from needles to the fanout are very short to keep their parasitic capacitance as low as possible. The supply voltages and currents provided by the subrepeater for the hybrid have to be adapted for only one chip (instead of 5 or ten for 2 hybrids).

The OnSiRoC module to which the repeater motherboard is connected runs the sequencer codes and digitizes the analog signals from the APC chip under test. The test setup is controlled by a Macintosh computer using the Labview [20]. Another Labview program, which differs from those mentioned in chapter 4, was written. It includes the data analysis too.

The oscilloscope is used to check the output analogue signal during the measurement. The output of "**RBO**" (read bit out) was directly displayed on the scope.

Test method

The test method checks for:

- gain (1/128) channels

- uniformity of storing locations (capacitors)
- full functionality

All pipeline capacitors of the storage array are used under usual running conditions. Therefore the homogeneity of their response has to be tested.

The method[2] chosen requires 32 different sequencer codes: for the readout of each of the 32 time slices. Advantages of this method are the high flexibility and the minimum hardware requirements. Each sequencer code generates a calibration pulse (for the APC) shifted accordingly to the time slice under investigation. An example of this pulse is shown in Fig. 5.5.

To have some statistics 10 events were taken for each time slice. Sometimes *bad events*[3] may occur. Therefore a special check of bad events is performed and if necessary a new event is measured. If such an event appears 5 times in series this APC is marked as "*Not Classified*". An average of the scanned amplitudes for all events is calculated after the data taking.

Data Analysis

The APC has one common calibration input for all channels (see Fig. 5.4) which is then AC coupled to the each channel through individual calibration capacitors (see Fig. 5.2). Calibration capacitors of four neighbouring channels have different nominal values 40, 80, 120, and 160 fF which give different charge injection (4 steps see Fig. 5.5). Therefore an array of 4x32x32 locations for data processing is needed.

Signal amplitudes are notated $\mathcal{A}^i_{j,k}$ will be used. Here $\mathcal{A}$ means the amplitude, i (1..4) is the level of charge calibration capacitor, j is the index of the recalculated channel[4] (1..32) and k denotes the time slice (1..32).

An example of calibration pulses of the raw data for $i = 1$ is shown in Fig. 5.6. A flat shape of this distribution is expected and all amplitudes have to be of a similar height over the whole pipeline. This behavior is confirmed by the plots in Fig. 5.6. The amplitudes rise linearly with the channel number, but the first channel and pipeline are systematically shifted to lower values. This effect is corrected in the analysis.

Amplitude fit

To suppress any systematic failures caused by capacitors having lower or

[2] Other possibilities can use e.g. random trigger or programmable trigger delay.

[3] *Bad event* means an event where OnSiRoC has no reasonable output.

[4] Real channel number $chn = i \cdot j$

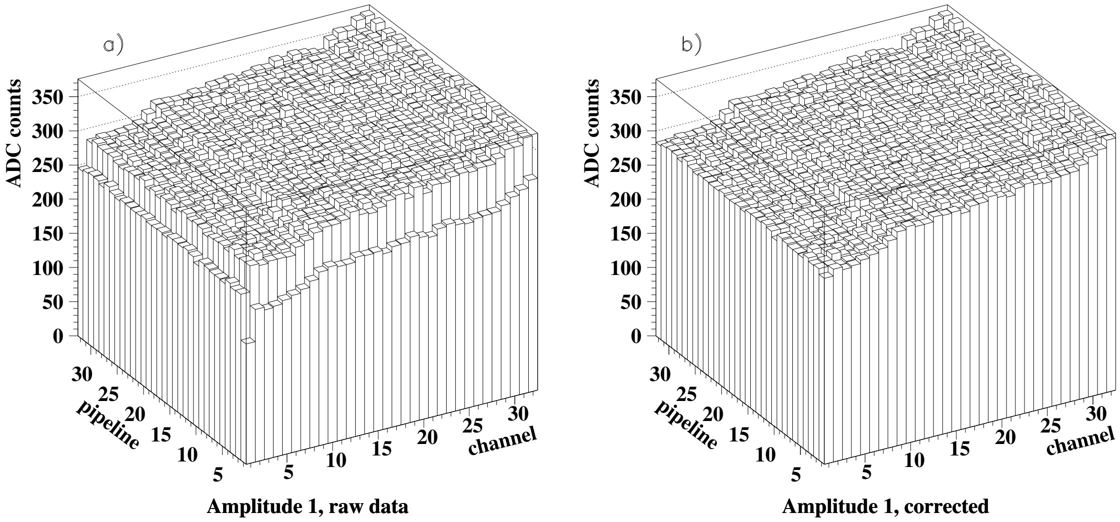

Figure 5.6: An example of the amplitudes in the first level: a) raw data b) after correction

higher response due to deviations or shortcuts, geometrical averages of all amplitudes in one channel is calculated:

$$\mathcal{P}^i_j = \sqrt[31]{\prod_{k=2}^{32} \mathcal{A}^i_{jk}} = \exp\left(\frac{1}{31}\sum_{k=2}^{32} \ln \mathcal{A}^i_{jk}\right) \tag{5.1}$$

The algorithm of the classification of APC chips is based on the assumption of the linearity of $\mathcal{P}^i_j$ as a function of the channel number j. Linear fits of $\mathcal{P}^i_j$ which give a slope a^i and an intercept b^i were performed for each level i separately. In case of a bad preamplifier all amplitudes of the corresponding channels are low and the geometrical average give a small contribution to the fit. The first channel in level one and first pipelines in all channels of amplitudes were excluded from the fit and were corrected in the next step.

Correction of the First pipeline and channel

A linear weighted formula is applied to fit the $\mathcal{A}^i_{j,1}$ ($j = 1..32$) except the first calibration pulse level, where the first channel is excluded (for $i = 1$; $j = 2..32$). Output parameters a^i_p, b^i_p are included in the calculation of the correction factor $\mathcal{F}_p$

$$\mathcal{F}_p = 16 \cdot \left(\frac{1}{4}\sum_{i=1}^{4} a^i - a^i_p\right) + \frac{1}{4}\sum_{i=1}^{4} b^i - b^i_p \tag{5.2}$$

which basically denotes the average of differences between the calculated values of amplitude $\mathcal{A}^i_{16,1}$ and $\mathcal{P}^i_{16}$ from corresponding fits. This factor is then added to each amplitude in the first pipeline to correct it to a proper value ($\mathcal{A}^i_{j=1..32,1} \rightarrow \mathcal{A}^i_{j=1..32,1} + \mathcal{F}_p$).

The first channel in the first level ($i = 1$) is corrected in similar way. The correction factor $\mathcal{F}_c$ is calculated using a linear weighted fit of $\mathcal{A}^1_{1,k}$ along the pipeline buffers where $k = 1..32$. The obtained parameters a_c, b_c are then included in the calculation of

$$\mathcal{F}_c = a^1 + b^1 - (16 \cdot a_c + b_c) \tag{5.3}$$

Again it corresponds to the difference between the calculated value of amplitude $\mathcal{A}^1_{1,16}$ and the extrapolated value of $\mathcal{P}^1_1$. This factor is then added to each amplitude in the first channel ($\mathcal{A}^1_{1,k=1..32} \rightarrow \mathcal{A}^1_{1,k=1..32} + \mathcal{F}_c$). The amplitudes before and after corrections of the first channel and pipeline are shown in Fig. 5.6a,b.

Search for bad capacitors

The differences $\mathcal{D}^i_{j,k}$ between the amplitudes and their plane fits are calculated

$$\mathcal{D}^i_{j,k} = \mathcal{A}^i_{j,k} - (a^i \cdot j + b^i) \tag{5.4}$$

The distributions of $\mathcal{D}^i_{j,k}$ made separately for each level i are fitted with Gaussian curves to obtain the mean d^i and sigma σ^i. The bad or dead capacitors are found using these parameters in the following way:

- A tolerance bandwidth $\sigma^i_{tot} = \sigma^i \oplus \sigma_{noise}$ was chosen (including noise and tolerable fluctuations of capacitances, the nominal value of σ_{noise} was 15 ADC counts).

- A *bad capacitor* is a capacitor whose $\mathcal{D}^i_{j,k}$ is not within $d^i \pm 3 \cdot \sigma^i_{tot}$

Bad capacitors are then capacitors with higher fluctuations. There may be capacitors with a position too far from the mean d^i of the Gaussian fits. The value of 400 ADC counts difference from d^i was chosen to mark a *dead capacitor*.

The next criterion was the linearity of the plane. Therefore an additional value called *response* was calculated from σ^i and compared with the reference σ_{ref} obtained from measurements of first few ten samples. *Response* $\mathcal{R}$ is then calculated from the relation

$$\mathcal{R} = 100 \frac{1}{4} \sum_{i=1}^{4} \frac{\sigma_{ref}}{\sigma^i} \tag{5.5}$$

If more than 20 capacitors are signed as bad or dead in one channel this channel is also marked as *bad channel*.

Classification

Having all qualifiers the APC chips were classified into seven main classes:

A - response is higher than 90%[5] , no bad capacitor

A2 - response lower than 90%, no bad capacitor

B - 1 to 4 bad capacitors, no dead capacitor

C - 5 to 10 bad capacitors, no dead capacitor

C2 - 1 dead capacitor and not more than 2 bad capacitors

D - all remaining chips

NC - Not Classified. This is a special class which appears if there were more than five *bad events* in consequence or after calculations if no reasonable results were found. It can be caused by a poor contact of the probe needles or by unexpected failures. Therefore two new classes were established:

- **MS** - Mechanical sample. Many failures occurred; for example the **RBO** output was not visible on the oscilloscope or the chip was not operational at all. Chips are used for tooling etc.

- **SF** - Special failures. These failures were not typical; for instance every forth channel was dead etc.; chips are kept for special purposes.

Using these classes all 3500 delivered APC chips were sorted except the mechanically damaged chips.

[5]This is the final value which varied during the measurement. The major part of the measurement was done using it.

Summary of Tests

The whole procedure of testing one chip took less than two minutes[6] in average. 3500 APC chips were checked with the described procedure in three and a half weeks. The results of the tests are shown in table 5.3.2.

Quality	A	A2	B	C	C2	D	SF	Mc + T
%	74	13	3	0.4	0.2	4	1.3	5

Table 5.1: Statistic of APC128 tests

The 74% of APC chips exhibits the required quality. This is a good production yield giving enough chips for both detectors, BST and FST.

5.4 Decoder Chip

The decoder chip is an ASIC especially designed for controlling of the APC128. It is fabricated in SACMOS1 technology. It performs a serial to parallel conversion of the incoming signals with different functions:

1. Providing the control signals for the APC128;
2. Sending a digital sequence of 32 bits as a calibration signal to the APC;
3. Providing the switches for slow control purposes e.g. temperature control; not used in BST and FST;
4. Regulating the analog current source for the APC preamplifier; not used in BST and FST;

The first function is used for normal running of BST and FST detectors.

The decoder chip is driven with two clock signals (**CLK1, CLK2**), **SR/OUT** signal, which switch two modes of the chip and **BIN** signal feeding the serial data into the chip.

[6]Most of this time was taken for the changing of the chips while the data acquisition and analysis take only 35 seconds.

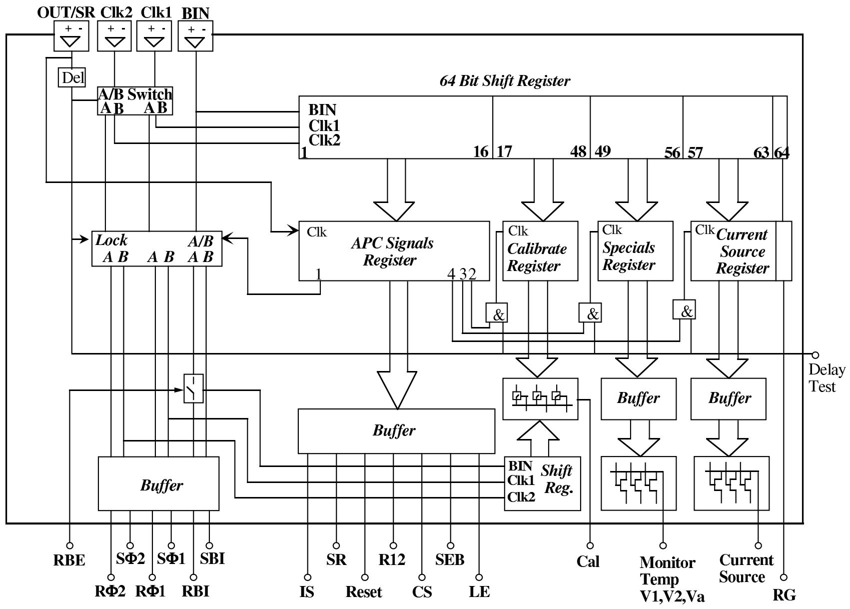

Figure 5.7: Decoder chip schematic view.

The first mode of operation is downloading of a data bit string containing up to 64 bits into the internal 64 bit shift register. The information from this register is then passed to other internal registers in the second mode depending on the first four bits in the shift register.

The switching between the **A/B** functions depends on the first bit. It means in fact the switching between Rϕ and Sϕ clocks.

The decision whether the calibration, control or current supply register will be filled depends on the next 3 bits. The remaining bits up to the bit 16 in the shift register are reserved for the control of the switches of the APC. This information from the shift register is transferred to the APC signal register every time the decoder is in the second mode.

All shift registers in the decoder as well as in the APC chips operate in the same way. Every register consist of cells which contain two inverters (logic level) and two auxiliary inverters which are connected in series. This schematic diagram forms a chain of "flip–flops" (see Fig. 5.8). Their logical status is overwritten by the input signal. The bit is shifted activating the clock signals **CLK1, CLK2** in the correct order. If the clocks are activated simultaneously the register is reset (so called "race through").

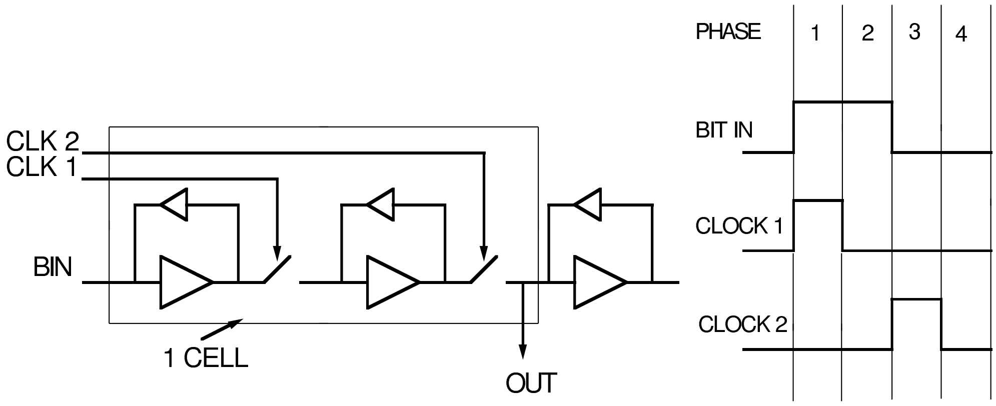

Figure 5.8: Schematic drawing of one cell of the shift register

5.4.1 Test of the decoder chips

The decoder plays a central role in the front–end readout. Any failure would cause failures to the APC chips and thus the total lost of data from the strips connected to the APC's driven by that particular decoder.

The decoder test was done in a similar way as the APC one. A fanout connects all cables to the probe card. It was glued to a modified hybrid with one APC chip. The contact to the decoder under test was provided by small needles placed on the probe card.

The OnSiRoC generated the signals for the decoder by the one of the sequencer codes from the APC tests. Calibration signals (see Fig. 5.5)were observed on the oscilloscope. If there was a signal visible without any deviations the functionality of the decoder was good. In the case of a malfunction of the decoder the signal would not appear at all because all main functions of the decoder were used and the missing of at least one would cause the readout chain failure.

More than 99% of all tested decoders were good.

Summary

This thesis presents a measured properties of the silicon sensors and the main readout components of the BST and FST detectors. They were designed to measure with high precision secondary charge particles tracks in the scattering of leptons and protons at the HERA collider.

The spatial resolutions of the r (ϕ) is expected to reach about $18\,\mu$m ($9\,\mu$m). The better kinematical acceptance and the good resolutions of both trackers will improve the detection of heavy quarks and the determination of the proton structure functions at low x and high Q^2. The detectors will be installed in spring 2001.

The results from tests of sensors presented in the thesis are obtained mainly from the measurement of properties of the ϕ strip sensors which have been delivered.

- The depletion voltages for the ϕ sensors are in the range 55 V – 75 V, for the r from 14 V to 35 V and for pad detectors about 40 V.

- The strip capacitances are measured in the strip tests by means of which mechanical failures can be found.

- The global properties of the whole detector modules are verified in the laser tests and modules which have bad functionality will be eliminated. Several test detector modules were tested in order to verify the overall performance of the laser setup and of the control and analysis program. The checks will continue in the autumn this year.

All tests are more or less automatically driven with several Labview programs. They were written to accelerate the tests, in order to the BST and FST construction was kept in the foreseen time schedule. The programs include control of various mechanical devices and also the mathematical data

analysis. Moreover they make possible to exclude failures caused by human factors.

The main readout components (APC128 and decoder chips) have been tested to avoid a loss of the detector efficiencies caused by their defects. Another Labview program was written to check APC128. Several sequencer codes for control of the chips with the OnSiRoC module were developed. They are used for various test options one of which is applied in the laser test.

More then 99% of decoders passed the tests. About 74% of 3500 APC chips which have been tested are of good quality and will be used for the completion of hybrids.

The various checks will continue in autumn 2000 in DESY–Zeuthen followed by the tests of the assembled BST and FST wheels including checks of the repeater electronics which will be delivered by Prague H1 group.

Appendix A

Strip–test program

As was mentioned the Labview program for the Strip–test was developed in the frame work of this thesis as well as the programs for the Laser–test, tests of the APC128 chip and the measurement of the depletion voltage.

Labview is a graphical programming tool [20]. Labview program consists of two main parts: the control panel (see Fig. A.1) where the controls and indicators of program (user interface) are presented and the programming window where the real program is written.

Every function is represented with the icon and the transfer of the data between functions can be done using the wires or variables. The order of steps is determined with the sequences frames. The similar frames are used for conditions or loops. There is a possibility to program user subroutines called subvi. The Labview package has also mathematic libraries for data analysis and the libraries for driving of interface of various devices (for detail see [20]). All these programming tools are used.

A short part of one of the strip test algorithms is showed bellow. The full version including the subvi's consists of more than 50 pages.

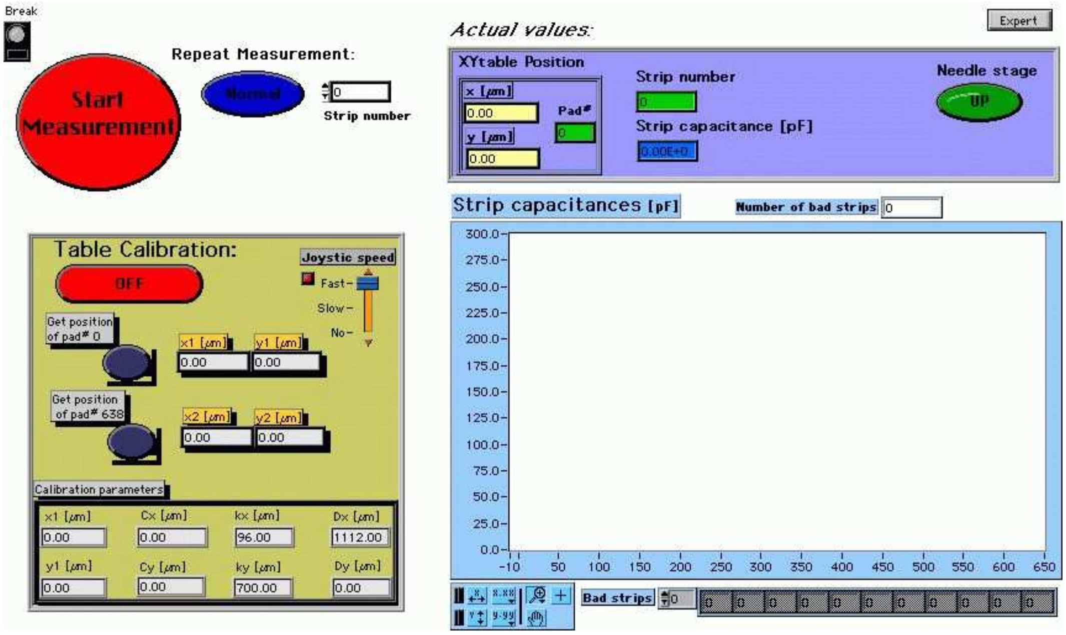

Figure A.1: User interface of the Strip–test program.

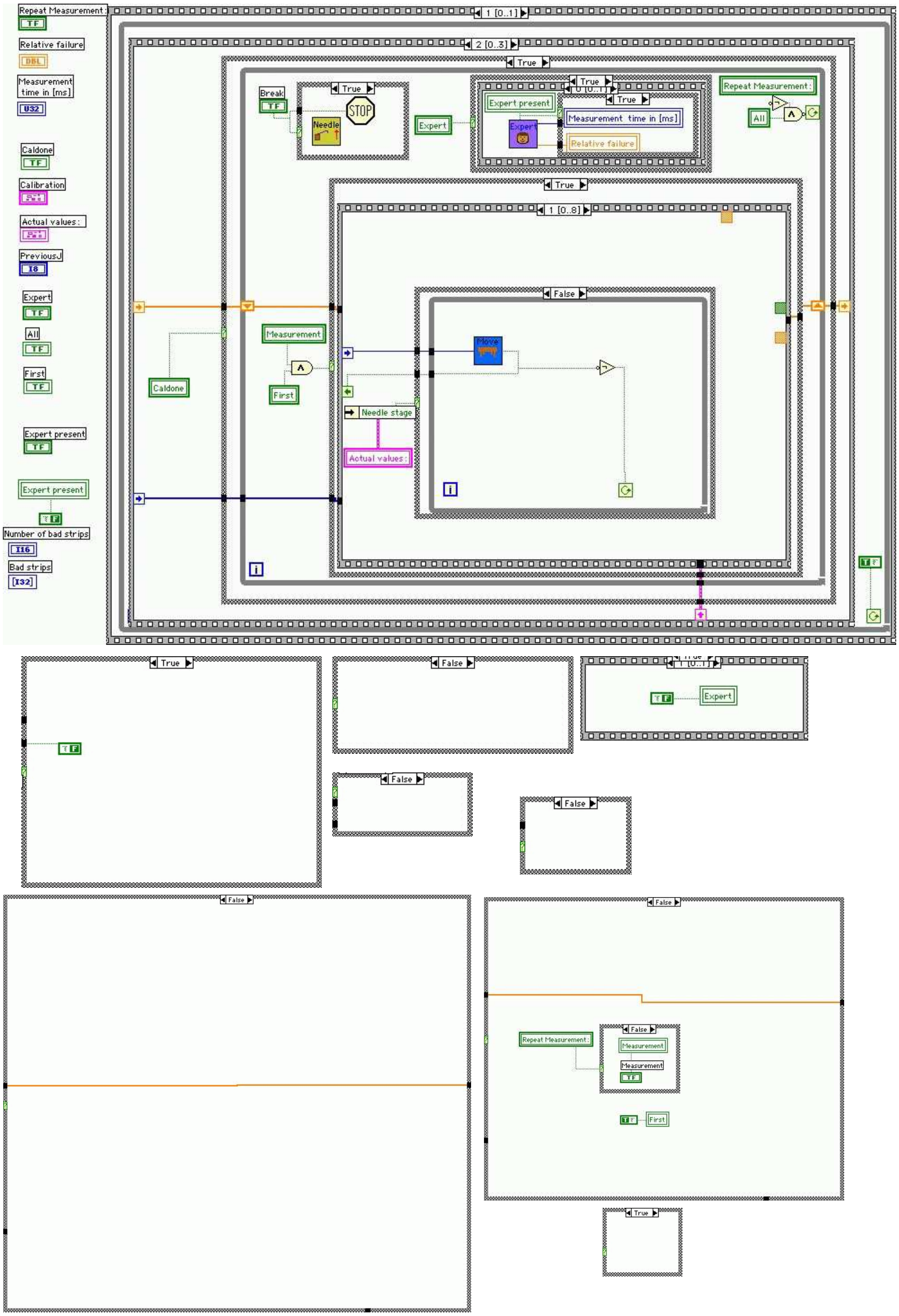

Repeat Measurement:
Relative failure
Measurement time in [ms]
Caldone
Calibration
Actual values:
PreviousJ
Expert
All
First
Expert present
Expert present
Number of bad strips
Bad strips
1 [0..1]
2 [0..3]
True
Break
True
STOP
Needle
Expert
True
0 [0..1]
True
Expert present
Measurement time in [ms]
Expert
Relative failure
Repeat Measurement:
All
True
1 [0..8]
False
Measurement
First
Caldone
Move
Needle stage
Actual values:
True
False
1 [0..1]
Expert
False
False
False
False
Repeat Measurement:
False
Measurement
Measurement
First
True

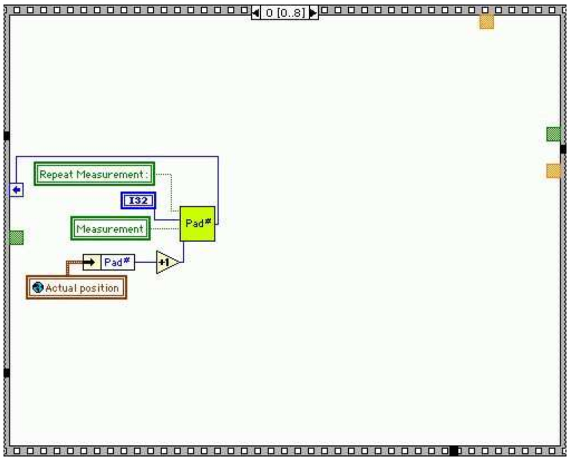
0 [0..8]
Repeat Measurement:
I32
Measurement
Pad#
Pad#
+1
Actual position

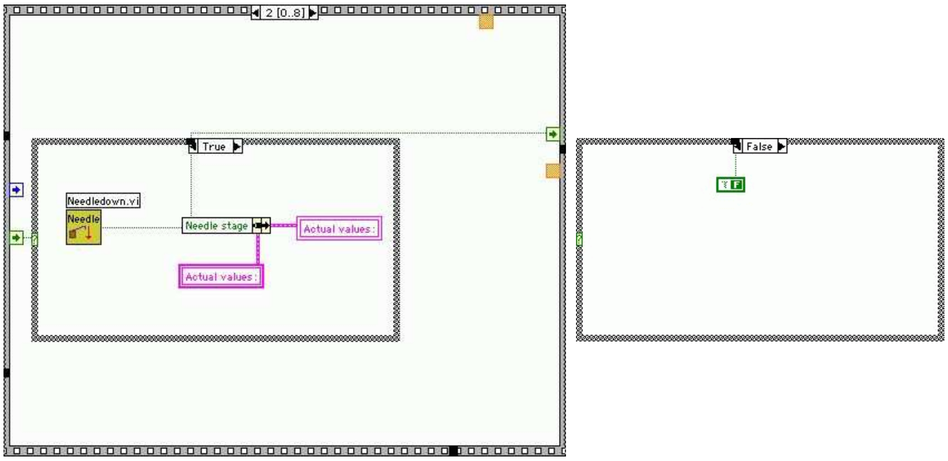
2 [0..8]
True
Needledown.vi
Needle
Needle stage
Actual values:
Actual values:
False

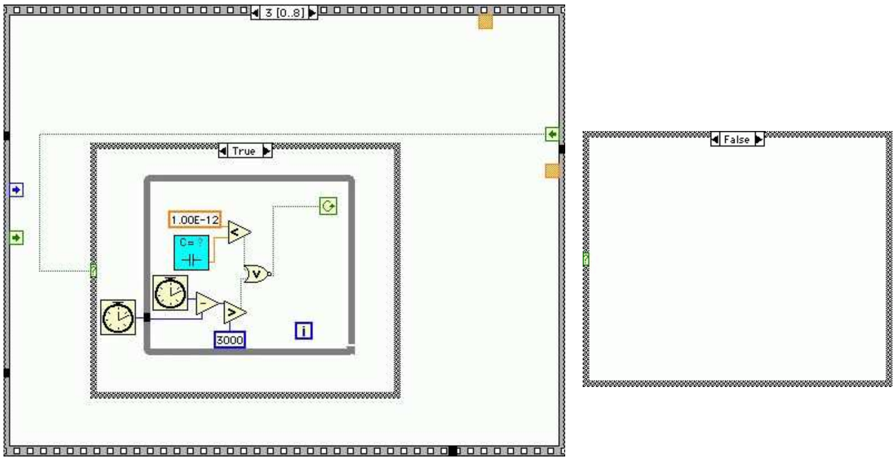
3 [0..8]
True
1.00E-12
C=
3000
i
False

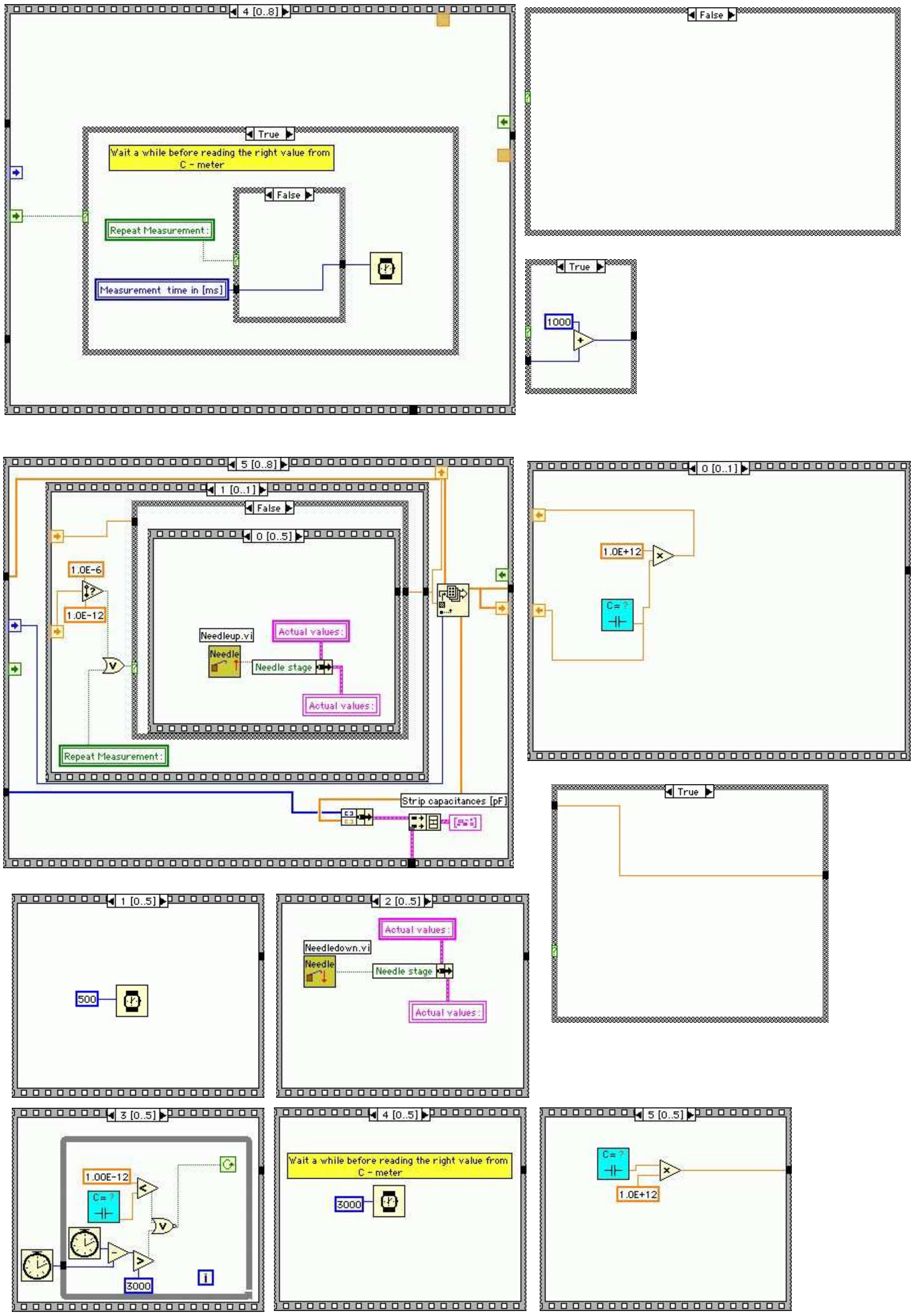
4 [0..8]
True
Wait a while before reading the right value from C - meter
False
Repeat Measurement:
Measurement time in [ms]
False
True
1000
5 [0..8]
1 [0..1]
False
0 [0..5]
1.0E-6
1.0E-12
Needleup.vi
Needle
Actual values:
Needle stage
Actual values:
Repeat Measurement:
Strip capacitances [pF]
0 [0..1]
1.0E+12
C= ?
True
1 [0..5]
500
2 [0..5]
Actual values:
Needledown.vi
Needle
Needle stage
Actual values:
3 [0..5]
1.00E-12
C= ?
3000
4 [0..5]
Wait a while before reading the right value from C - meter
3000
5 [0..5]
C= ?
1.0E+12

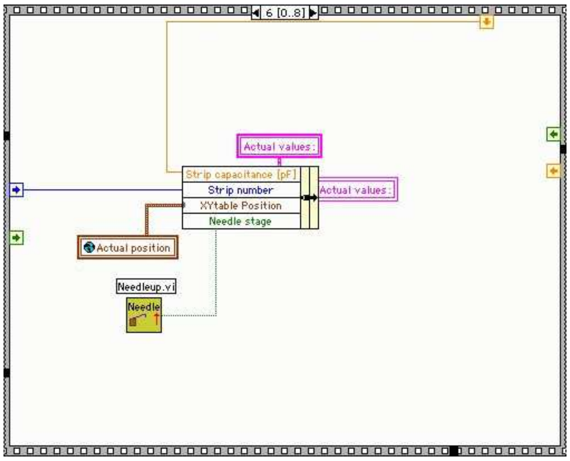
6 [0..8]
Actual values:
Strip capacitance [pF]
Strip number
XYtable Position
Needle stage
Actual values:
Actual position
Needleup.vi
Needle

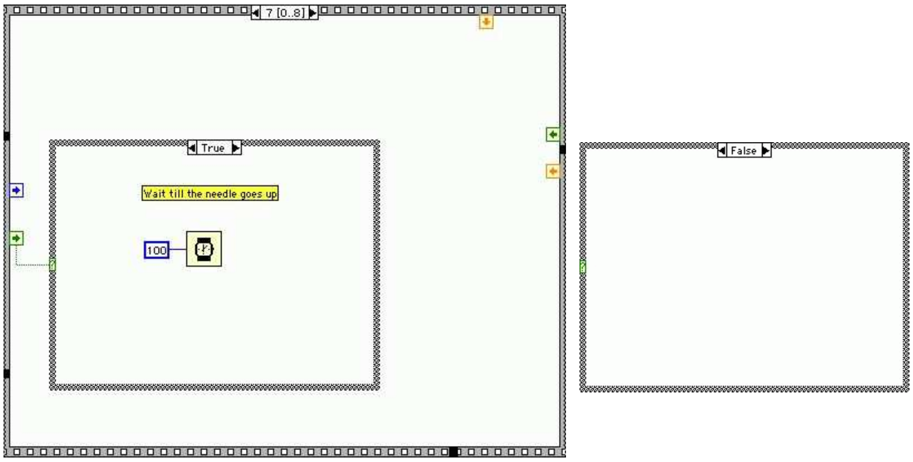
7 [0..8]
True
Wait till the needle goes up
100
False

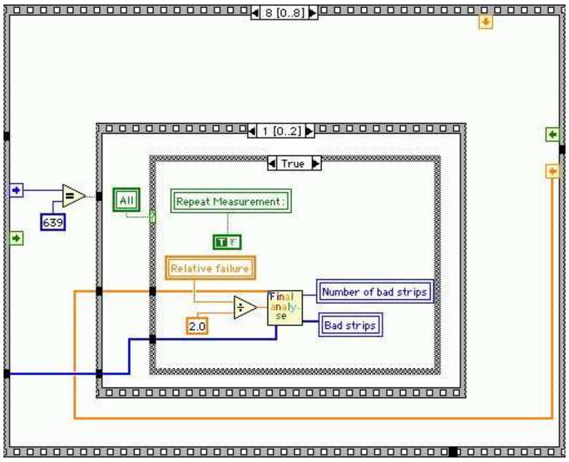
8 [0..8]
1 [0..2]
True
All
Repeat Measurement:
639
Relative failure
Number of bad strips
Final analyse
2.0
Bad strips

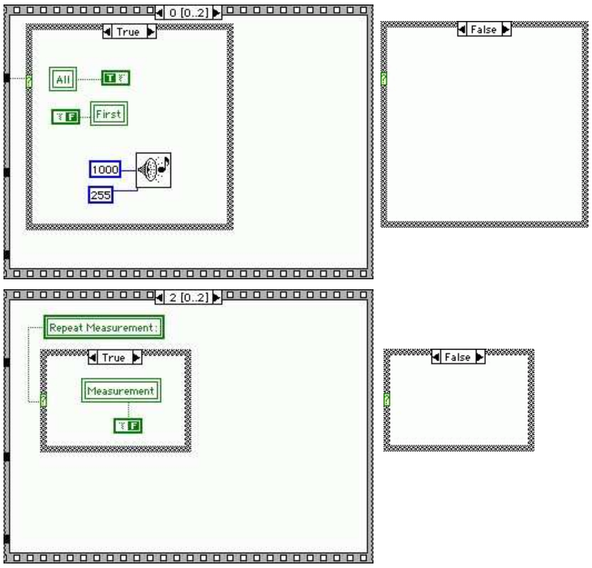
0 [0..2]
True
All
First
1000
255
False
2 [0..2]
Repeat Measurement:
True
Measurement
False

Appendix B

Sequencer code

Sequencer code is a programmable code for the control of the APC128 chip using the OnSiRoC module.

	First mode	Second mode
Bit number	**Function 0/1**	**Function 0/1**
1	$S\Phi/R\Phi$ clock	CLK1
2	Calibration register on/off	CLK2
3	Control register on/off	BIN
4	Current supply register on/off	SR/OUT
5	Reset close/open	Clock chopper
6	IS close/open	SQD out
7	SR close/open	SQD out
8	R12 close/open	SQD out
9	CS close/open	Clock Fast/Slow, Slow = $\frac{10}{n+1}$MHz
10	SEB high/low	Pipeline counter
11	LE high/low	Channel counter 1 (CC1)
12	RBE early on/off	Channel counter 2 (CC2)
13	not used	OVFL SBI
14	not used	SQD13
15	RBE late on/off	Sequencer memory low/high
16	not used	SQD15

Table B.1: Control bits of the sequencer code (counting from right in code).

The commands are represented by binary numbers of 16 bit length. Two modes of decoder chip operation has to be distinguished (see section 5.4). In the first mode the 64 bit shift register of the decoder is downloaded (command SR_IN). The description of the first 16 bits for the APC128 control is shown in table B. In the second mode the first four bits are used as inputs of decoder and the remaining bits are reserved for some OnSiRoC functions (see table B).

The sequencer code consists at least of two phases (command ROUTINE) (see 5.2), from which are selected readout and sample phase using their numbers. Each phase ended with the corresponding trigger bit and LOOP. To simplify the orientation in the code defined MACROS and multiple INSERT are used. Moreover there is a possibility to use comments in brackets.

An example of the parts of the sequencer code which used in Laser–test follows:

```
{ OnSiRoC II Sequencer code for Laser test setup, readout of one pipeline
buffer 5,  640 channels}
{    19.4. 2000 Miroslav Nozicka }
{====================================================================}
{       }
{         Part 1: basic Sequencer MACROs                             }
{        }
{====================================================================}
{-----------------------------------------------------------------------}
{  Race through macros  }
{-----------------------------------------------------------------------}
MACRO  Reset_APC_SR  0000 0000 0001 1011 ENDMACRO
MACRO  Reset_APC_SR_Slow 0000 0001 0001 1011 ENDMACRO
MACRO Set_Latches  0000 0000 0001 1111 ENDMACRO
MACRO Set_Latches_Slow 0000 0001 0001 1111 ENDMACRO
{-----------------------------------------------------------------------}
{  Clocks Macros:  }
{-----------------------------------------------------------------------}
MACRO  Phi_1_Fast 0000 0010 0000 1001 ENDMACRO
MACRO  Phi_2_Fast 0000 0010 0000 1010 ENDMACRO
MACRO  Phi_1_SBI_Fast 0000 0010 0000 1101 ENDMACRO
MACRO  Phi_1_Slow_SBI 0000 0011 0000 1101   ENDMACRO
MACRO  Phi_2_Slow 0000 0011 0000 1010   ENDMACRO
```

```
MACRO  Phi_1_Slow 0000 0011 0000 1001   ENDMACRO
{- - - - - - - - - - - - - - - - - - - - - - - - - - - - - - - - - - - - -}
{ Shift of bits in the register }
{- - - - - - - - - - - - - - - - - - - - - - - - - - - - - - - - - - - - -}
MACRO  Clock_Fast Phi_1_Fast
Phi_2_Fast ENDMACRO
MACRO  Clock_SBI_Fast Phi_1_SBI_Fast
Phi_2_Fast ENDMACRO
MACRO  Clock_Slow_SBI Phi_1_Slow_SBI
Phi_2_Slow ENDMACRO
MACRO  Clock_Slow Phi_1_Slow
Phi_2_Slow ENDMACRO
...

...
ROUTINE $1 Scan_Mode_Laser
INSERT 3 TIMES Zero_Fast ENDINSERT
SR_IN 0   ENDSR_IN
SR_IN 010 0000 ENDSR_IN
SR_IN 1111 1111 ENDSR_IN
SR_IN 0000 0000 0000 0000
0000 0000 0000 0000 ENDSR_IN
SR_IN 1 1111 011 0000 0000 ENDSR_IN
INSERT 2 TIMES Zero_Fast_Out ENDINSERT
INSERT 64 TIMES Reset_APC_SR   ENDINSERT
INSERT 2 TIMES Zero_Fast ENDINSERT
SR_IN 1 0110 011 0000 1111 ENDSR_IN
INSERT 2 TIMES Zero_Fast_Out ENDINSERT
INSERT 128 TIMES Set_Latches ENDINSERT
       0000 0000 0001 0111
INSERT 2 TIMES Zero_Fast ENDINSERT
SR_IN 1 0110 011 0001 1110 ENDSR_IN
INSERT 2 TIMES Zero_Fast_Out ENDINSERT
SQD13
LOOP
Laser_Trigger
Pipe_Loop_Fast_SBI
ENDLOOP
```

```
{-------------------------------------------------------------------------}

ROUTINE $2  ReadOut
INSERT 2 TIMES Zero_Slow_Out ENDINSERT
0000 0001 0000 1010
INSERT 2 TIMES Zero_Slow ENDINSERT
Scope_Trigger
INSERT 2 TIMES Zero_Slow ENDINSERT
{ == 1 == }
{Readout Setup Phase}
SR_IN 0000 0000 0000 0000
0000 0000 0000 0000 ENDSR_IN
SR_IN 1 0110 001 0001 1100 ENDSR_IN
INSERT 2 TIMES Zero_Slow_Out ENDINSERT
INSERT 2 TIMES Zero_Slow ENDINSERT
{ == 2 == }
{Readout Init Phase}
...

...
INSERT 2 TIMES Zero_Slow ENDINSERT
SR_IN 1 0110 001 1111 1111 ENDSR_IN
INSERT 6 TIMES Zero_Slow_Out ENDINSERT
One_Strip_RO_RBI_CC1
One_Strip_RO_CC1
INSERT 638 TIMES  One_Strip_RO_CC12  ENDINSERT
One_Strip_RO_CC2
One_Strip_RO_CC2
INSERT 100 TIMES Zero_Slow_Out ENDINSERT
INSERT 2 TIMES RO_End ENDINSERT
{ === 5 ===}
{At the End init and Sample loop}
INSERT 2 TIMES Zero_Fast_Out ENDINSERT
INSERT 2 TIMES Zero_Fast ENDINSERT
SR_IN 1 0110 011 0000 1111 ENDSR_IN
INSERT 2 TIMES Zero_Fast_Out ENDINSERT
INSERT 128 TIMES Set_Latches ENDINSERT
0000 0000 0001 0111
```

```
INSERT 2 TIMES Zero_Fast ENDINSERT
SR_IN 1 0110 011 0001 1110 ENDSR_IN
INSERT 2 TIMES Zero_Fast_Out ENDINSERT
INSERT 2 TIMES Zero_Fast ENDINSERT
SR_IN 1 0110 011 0001 1110 ENDSR_IN
INSERT 2 TIMES Zero_Fast_Out ENDINSERT
LOOP
Pipe_Loop_Fast_SBI
ENDLOOP

END
```

Bibliography

[1] J. Chýla, Quarks, partons and Quantum Chromodynamics, Lecture notes available at http://www-hep.fzu.cz/Theory/notes/text.ps.gz

[2] H1 colaboration, A Measurement of the Proton Structure Function $F_2(x, Q^2)$, hep-ex/9503001

[3] V. Arkadov, Measurement of the Structure Functions F_2 and F_L at Low x, Nuclear Physics B 79 (1999) 179-181

[4] M. Klein, Structure Functions in Deep Inellastic Lepton-Nucleon Scattering, hep-ex/0001059

[5] T. Doyle, Structure functions, hep-ex/9812030

[6] B.Foster, Deep Inelastic Scattering at HERA, International Journal of Modern Physics A Vol.13 No.10 (1998)

[7] A. A. Glazov, Measurement of the Structure Funtions $F_2(x, Q^2)$ and $F_L(x, Q^2)$ with H1 Detector at HERA, Phd. Thesis Humbolt University Berlin

[8] V. V. Arkadov, Measurement of the Deep–Inelastic ep Scattering Cross Section using the Backward Silicon Tracker at the H1 Detector at HERA, Phd. Thesis Humbolt University Berlin

[9] I. Abt et al., The tracking, calorimeter and muon detectors of the H1 experiment at HERA, Nucl. Instr. and Meth. A386 (1997) 348

[10] I. Abt et al., The H1 Detector at HERA, Internal Report DESY H1-96-01, Hamburg (1996)

[11] H1 SPACAL group, Performance of an Electromagnetic Lead/Scintillating-Fibre Calorimeter for the H1 Detector, Nucl. Instr. and Meth. A374 (1996) 149-156

[12] U. Bassler and G. Bernardi, On the Kinematic Reconstruction of Deep Inelastic Scattering at HERA: the Σ Method, hep-ex/9412004

[13] Markus Kausch, The Silicon Microvertex Detector of the H1 Experiment: Readout, Event Reconstruction and Studies on Heavy Quark Decays, Phd. Thesis Hamburg University

[14] U. Schneekloth, The HERA Luminosity Upgrade, nonpublished DESY library

[15] W.R.Leo, Techniques for Nuclear and Particle Physics Experiments, Springer–Verlag Berlin 1987

[16] Particle Physics booklet, Springer–Verlag 1998

[17] Measurement of D^* Meson Cross section at Hera and Determination of the Gluon Density using NLO QCD, H1–Collaboration, hep-ex/9812023

[18] Measurement of Open Beauty Production at HERA, H1–Collaboration, hep-ex/9909029

[19] V. Comichau et al., Test of a high resolution drift chamber prototype, Nucl. Instr. and Meth. A235 (1985) 267-278

[20] Labview – Graphical Programming Environment, National Instruments

[21] J.Bürger et al.,Online readout and control unit for high–speed/high resolution readout of silicon tracking detectors, Nucl.Instr. and Meth. A386 (1997) 269-279

[22] A Forward Silicon Tracker for H1, W. Braunschweig et. al., H1 internal note H1-02/99 563